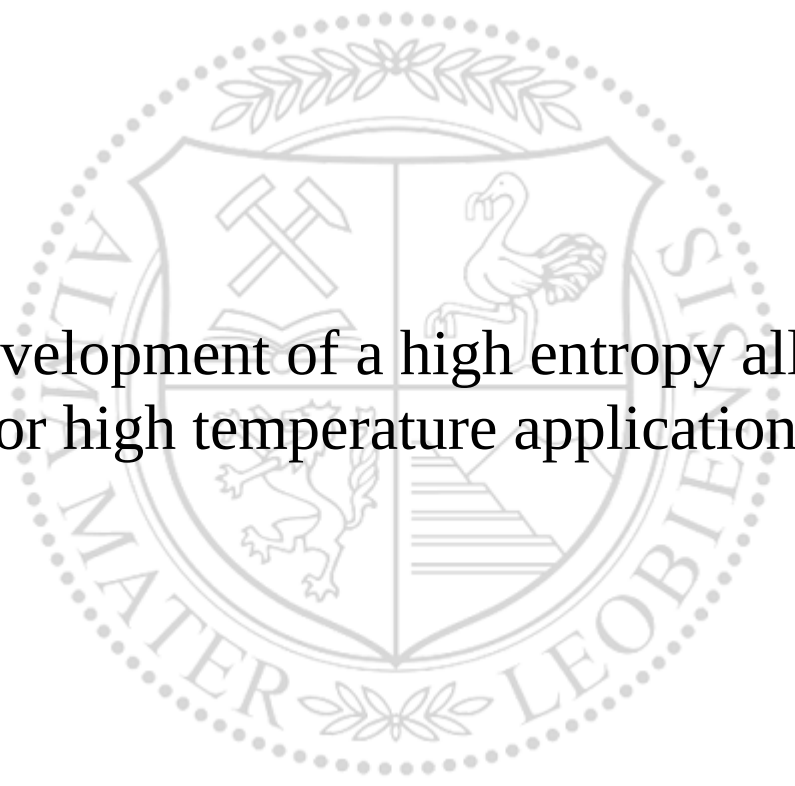




Chair of Physical Metallurgy and Metallic Materials

Master's Thesis



Development of a high entropy alloy
for high temperature applications

Stefan Zeisl, BSc

March 2020



EIDESSTATTLICHE ERKLÄRUNG

Ich erkläre an Eides statt, dass ich diese Arbeit selbständig verfasst, andere als die angegebenen Quellen und Hilfsmittel nicht benutzt, und mich auch sonst keiner unerlaubten Hilfsmittel bedient habe.

Ich erkläre, dass ich die Richtlinien des Senats der Montanuniversität Leoben zu "Gute wissenschaftliche Praxis" gelesen, verstanden und befolgt habe.

Weiters erkläre ich, dass die elektronische und gedruckte Version der eingereichten wissenschaftlichen Abschlussarbeit formal und inhaltlich identisch sind.

Datum 20.02.2020

Unterschrift Verfasser/in
Stefan, Zeisl

I hereby declare in lieu of oath that I wrote this thesis by myself, without the help of outside sources, performed all the experiments by myself and used none other than the cited literature.

Stefan Zeisl

Acknowledgements

I want to thank Prof. Helmut Clemens and the Chair of Physical Metallurgy and Metallic Materials for providing me with this exciting topic for my master thesis and for providing state of the art instruments and research facilities. To Prof. Helmut Clemens I would like to give a further special thanks for aiding with the correction of this thesis in a time-critical situation.

My gratitude also goes to my supervisor Prof. Svea Mayer who always had time to discuss the newest findings and who always pointed me in the right direction. But most of all, I am thankful that she always managed to encourage and motivate me when I was feeling overwhelmed or when I thought I had worked myself into a corner.

Furthermore I want to thank the technical staff of the department, namely Silvia Pölzl and Thomas Fischer, and also Dipl. Ing. David Wimmeler and Dipl. Ing. Reinhold Wartbichler for helping me out with some of the instruments and for helping me with technical details.

Finally, I want to thank my parents for their unconditional support throughout my whole career path, without whom I would not be where I am today, as they always managed to pick me up when things seemed desperate and helped me to put things into perspective.

Abstract

High-entropy alloys are a relatively young class of metallic materials and have gained increasing popularity in research within the last decade. The regime of high-entropy alloys is vast and largely undiscovered, making it possible that there might be hidden materials with exceptional properties. In this master thesis a series of high-entropy alloys, based on the equiatomic compositions of AlTiMnNbV and AlTiMoNbV, are tested on their ability to form a solid solution, their thermal stability and their microstructural evolution in response to heat treatments. The goal is to find an alloy which forms a single-phase solid solution and shows reasonable stability at higher temperatures.

Kurzfassung

Hochentropielegierungen sind eine relativ junge Klasse metallischer Materialien, deren Popularität in der Forschung in den letzten zehn Jahren stark zugenommen hat. Das Gebiet der Hochentropielegierungen ist größtenteils unerforscht, wobei die Hoffnung besteht, dass eine Materialkombination mit außerordentlichen Eigenschaften zu finden ist. Im Rahmen dieser Arbeit werden verschiedene Legierungen auf Basis der äquiatomaren Zusammensetzungen AlTiMnNbV und AlTiMoNbV auf ihre Fähigkeit untersucht, einen Mischkristall zu bilden. Weiters wird überprüft, ob diese Mischkristalle thermisch stabil sind und wie sich die Mikrostruktur im Zuge verschiedener Wärmebehandlungen entwickelt. Ziel dieser Arbeit ist es, eine Legierung zu finden, die sowohl einen Mischkristall bildet, als auch eine Mikrostruktur-Stabilität bei höheren Temperaturen zeigt.

Contents

Affidavit	ii
Acknowledgements	iv
Abstract and Kurzfassung	v
Table of Contents	vi
List of abbreviations	vii
1 Introduction	1
1.1 Motivation	1
1.2 Aim of this thesis	1
2 High-entropy alloys	2
2.1 Thermodynamic fundamentals	2
2.2 Definition of high-entropy alloys	3
2.3 Four HEA core-effects	4
2.4 Properties of HEAs	6
2.5 The AlTi-X-NbV system	9
3 Materials and experimental methods	10
3.1 Selection of materials	10
3.2 Microstructural characterization	10
3.3 Crystal structure analysis	12
3.4 Thermal analysis	13
3.5 Density and hardness	14
3.6 Severe plastic deformation	14
4 Results and discussion	16
4.1 AlTiMoNbV	16
4.2 AlTiMnNbV	21
4.3 $\text{Al}_{20}\text{Ti}_{30}\text{Mn}_{10}\text{Nb}_{20}\text{V}_{20}$	25
4.4 $\text{Al}_{20}\text{Ti}_{10}\text{Mn}_{30}\text{Nb}_{20}\text{V}_{20}$	35
4.5 Further thoughts on the $\text{AlTi}_x\text{Mn}_y\text{NbV}$ system	38
5 Conclusions	41
Appendix	a

List of abbreviations

APT	atom probe tomography
bcc	body-centered cubic
BSE	backscattered electron
CCA	complex concentrated alloy
DSC	differential scanning calorimetry
EBSD	electron backscatter diffraction
fcc	face-centered cubic
hcp	hexagonal close-packed
HEA	high-entropy alloy
HPT	high-pressure torsion
SEM	scanning electron microscopy
SPD	severe plastic deformation
TEM	transmission electron microscopy
XRD	X-ray diffraction

1 Introduction

1.1 Motivation

High-entropy alloys (HEAs) are a relatively new class of materials which rapidly grew popular in scientific research over the last decade. The idea behind this type of alloys is as follows: five or more metallic elements are taken in equiatomic quantities and mixed together, in the hope that they are completely miscible and form a microstructure with a single solid-solution phase. By thoroughly planning what kind of elements are used in the alloy, the searched for single-phase materials can often be achieved, whereupon the most common crystal structures are face-centered cubic (fcc) and body-centered cubic (bcc) [1, 2].

The alloy which has attracted increasing attention to HEAs was B. Cantor's FeCrMnNiCo-alloy, the so-called Cantor-alloy [3]. Cantor has provided research output for a previously very underrepresented type of alloys. He found that his Cantor-alloy not only forms a single-phase microstructure, but also possesses reasonable strength and ductility at room temperature [3]. Since then an insurmountable amount of new high-entropy alloys have been produced and researched, as well as mathematical models and simulations were and are being created to predict the formation of single-phase high-entropy alloys [4–6].

1.2 Aim of this thesis

The goal of this thesis is to start from a given selection of elements based on the so-called TNM alloy, which was developed by the working group "Phase Transformation and High-Temperature Materials" at the department of Materials Science, Montanuniversität Leoben, and find a high-entropy alloy which satisfies above requirements and can be used as a starting point for further research. To do so, the first step is to find if, or under which circumstances, a single-phase microstructure can be obtained for a given alloy. The second step is to take the HEA and test it if the solid solution is stable as a single phase after long time at higher temperatures and determine the circumstances under which the formation of secondary phases and demixing occur.

2 High-entropy alloys

2.1 Thermodynamic fundamentals

The miscibility of two or more substances is determined by the change in the Gibbs free energy $\Delta_{mix}G$ of mixing. This change of energy is made up of the change in enthalpy $\Delta_{mix}H$, which can be positive as well as negative, and the change in entropy $\Delta_{mix}S$, which is always positive and promotes the miscibility of the substances [7].

$$\Delta_{mix}G = \Delta_{mix}H - T \cdot \Delta_{mix}S \quad (2.1)$$

There are three ways in which a solution can be described:

- ideal,
- regular or
- sub-regular solution.

The definition of an ideal solution states that the interactions between solute and solvent molecules are the same as those between the molecules of each substance itself. Since the enthalpy of mixing is calculated as the difference of the interaction energies, it is zero for an ideal solution $\Delta_{mix}H = 0$. The regular solution is a more realistic approach in which the difference in the interaction energy between the solute and solvent molecules is considered to be non-zero. Both models have in common that the entropy of mixing is [6]:

$$\Delta_{mix}S = -n \cdot R \cdot \sum_{i=1}^m x_i \cdot \ln x_i \quad (2.2)$$

Where R is the ideal gas constant, n the total number of moles and total randomness for the distribution of solvent and solute atoms is assumed.

The reality is, and this is especially true for solid solutions, that both the ideal and regular solutions do not satisfy the requirements we need for high-entropy alloys [8]. First of all, atoms are not really randomly distributed as there is always chemical short-range order to a certain degree which is responsible for decreasing the entropy of mixing [8]. Furthermore a difference in the enthalpy of mixing is observed in comparison to the regular solution. Both effects can lead to a shift of the minimum of $\Delta_{mix}G$ from an equiatomic to a non-equiatomic composition, which means that the most stable mixture is not necessarily equiatomic [1].

2.2 Definition of high-entropy alloys

High-entropy alloys are a relatively new class of metallic materials. Their discovery goes back to several papers by B. Cantor and J. W. Yeh et al. [3, 9]. Generally speaking one can classify a metallic alloy as high-entropy alloy if it satisfies the following criteria [2]:

- They are composed of five or more elements.
- All alloying elements are present in an equiatomic concentration.
- A homogeneous single-phase material is formed wherein all elements are in solid solution (see Fig. 2.1).

These criteria are, however, loosely defined, because oftentimes alloys with non-equiatomic concentrations or only four elements are also regarded as high-entropy alloys. In recent materials science research, a concept of complex concentrated alloys (CCAs) is used to describe multi-component alloys close to the center of the composition space [10].

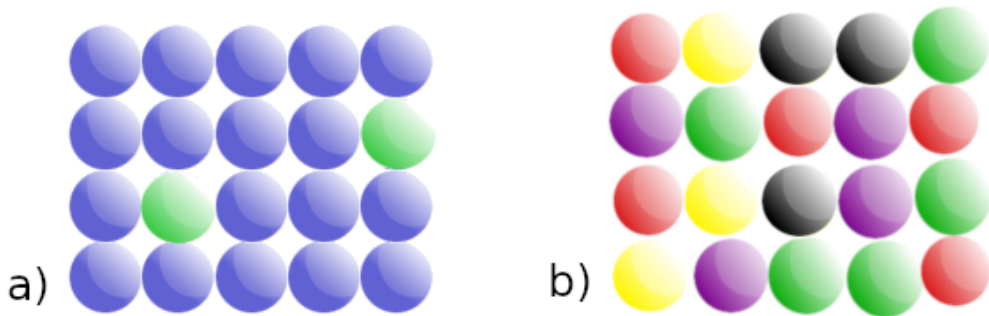


Figure 2.1: The distribution of different alloying elements, as represented by different colors, in a) a typical metallic alloy and b) in a high-entropy alloy.

A fact that proves to be a challenge in modern materials science is the sheer number of possible HEA variations. Even if you limit yourself to 28 transition metals of the fourth, fifth and sixth period (without Lanthanoids and Hg) along with aluminium, 29 elements in sum, you still get a very large number of possible variations [1, 10]:

$$N = \binom{29}{5} = 1.18 \cdot 10^5 \quad (2.3)$$

Because of this fact, ab-initio calculations are oftentimes used to determine if the solid solution shows the lowest energy of formation and are thus a first step to find new candidates for high-entropy alloys [5].

2.3 Four HEA core-effects

Recent papers suggested that HEAs have a set of desirable and unique properties, which were condensed into the four so-called core-effects [10]. However, other studies have found that some of these four core-effects are not as pronounced or play less of a role in the properties of HEAs than previously thought. The core-effects will be explained and critically reviewed in the coming paragraphs, but firstly they are called as follows [1]:

- High entropy effect,
- Lattice distortion effect,
- Sluggish diffusion effect and
- “Cocktail” effect.

2.3.1 High entropy effect

The arguably most important, and thus name-giving, core-effect proposes that a high configurational entropy in near-equiatomic alloys with five or more elements stabilizes a solid solution in contrast to the formation of intermetallic compounds [2]. The configurational entropy, however, is only one part of the whole. When we look at the entropy of a material we also need to consider the other types of entropy, for example electronic, magnetic and vibrational terms, which contribute to the overall change in entropy too. But these contributions are often disregarded, the reason for this is explained in the next paragraphs. As already mentioned, the other types of entropy are as follows [1, 11]:

- Electronic,
- magnetic and
- vibrational entropy.

In contrast to the configurational entropy, the electronic and magnetic entropy are often disregarded, which is due to the fact that their contribution to the overall change in entropy is typically relatively low [1]. The absolute value of the vibrational entropy is oftentimes larger than the entropy of mixing itself, but when we look at the overall change in vibrational entropy between parent and product phases, it is, again, small enough to be disregarded [1]. Another very important factor to consider, regarding the change of entropy, is that oftentimes the entropy of mixing for an ideal solid solution is

used. This can be a good approximation, but for high-entropy alloys the current state of knowledge suggests that chemical short-range order might play a major role in the properties of HEAs. Thus, the change in entropy given by the model of an ideal mixture must be higher than the change of entropy under non-standard conditions [8].

2.3.2 Lattice distortion effect

As is usual when dealing with substitutional solid solutions, there is a severe distortion of the lattice in the vicinity of the solute atom. This effect is strongly pronounced in HEAs as many different sized atoms are sharing a lattice with each other [1]. Lattice distortion, or atomic size misfit, is one of the main contributing factors to solid solution strengthening [12, 13], consequentially influencing the mechanical properties by the strongly distorted nature of the lattice of a HEA. Furthermore, electrical and thermal properties are influenced as well. The determination of the magnitude in which the lattice distortion affects the aforementioned properties is a challenging task, as this effect is not easily distinguished from other effects which might be influencing the same properties [1].

2.3.3 Sluggish diffusion effect

Reference [1] proposes that, generally, HEAs have a very slow diffusion behaviour for substitutional elements, as it was first observed in the work of Yeh et al. [9]. Recent research papers have shown that the sluggish-diffusion effect is not as strongly pronounced as firstly thought. Dabrowa et al. [14] found that many HEA systems do not show slower diffusion kinetics than conventional alloys, compared at both homologous and absolute temperature. However, they also found that there is a correlation when the alloy has Manganese as one of the alloying elements, showing a sluggish diffusion behaviour, but this correlation was only found for homologous temperatures [14].

As diffusion is the main mechanism of for e.g. phase transformations and high-temperature creep, slow diffusion kinetics can have a positive effect on both phase stability and high-temperature mechanical properties.

2.3.4 Cocktail effect

The cocktail effect has its roots in the field of metallic glasses and super-elastic metals. This group of materials oftentimes have very complex compositions with many alloying

elements. In short, the cocktail effect is a description of the non-linear, unexpected results that can occur from unusual combinations [1, 2].

2.4 Properties of HEAs

2.4.1 Solid solution strengthening

Solid solution strengthening works by hindering the movement of dislocations due to local lattice distortion in the vicinity of a solute atom. The elastic interaction effects (i.e. size and modulus effect) dominate for most crystalline materials. There are three different types of interactions which can be described [15]:

- Parelatic interaction (size interaction): describes the interaction between the stress field around the solute atom and the stress field of the dislocation.
- Dielastic interaction (inhomogeneity interaction): describes the interaction due to a difference in the shear modulus of solvent and solute atom, which has an effect on the line energy of a dislocation.
- Chemical interaction: the alloying of metals reduces the stacking fault energy, which leads to a larger dissociation into a pair of partial dislocations, and thus, to a hindrance of cross-slipping.

In conventional alloys the solid solution strengthening effect can be described by the Fleischer model [13] and the Labusch model [16], for dilute concentrations ($c < 1 \text{ at\%}$) and concentrated solid solutions, respectively [12]. Both models correlate an increase in the strengthening effect to an increase in the concentration of the solute atom (both of which evaluate the strengthening through statistical combination of the interaction between dislocation and solute atom), whereupon the effectiveness of the strengthening is dependent on the difference in atomic size and modulus between foreign and parent atom [12].

As HEAs present a special case due to their high concentrations of the constituent elements, neither the Fleischer model, nor the Labusch model are capable of describing the mechanisms behind solid solution strengthening in HEAs. In recent years models were created which seek to fill this gap in understanding. One example of such a model is the effective medium concept developed by Varvenne et al. [17], which describes that the possible interaction between solute atoms inside an effective average medium which interacts with dislocations. One of the proposed mechanisms is that dislocation lines develop a wavy structure to minimize the energy, which is made possible

by the favourable solute interactions. This energy gain increases the force which must be overcome to move the dislocation, giving rise to an addition to the solute solution strengthening effect [12].

The effect of the randomness of the distribution of elements within the crystal lattice has on the intrinsic strength of an high-entropy alloy was studied by Zhang et al. [18]. They modified the stochastic Peierls-Nabarro model by introducing a random variable to account for the atomic scale randomness of the distribution of elements and for the formation of short-range order. They found that the alloy strength increases as a function of the standard-deviation and the correlation length of the randomness.

2.4.2 Single-phase microstructures

One of the main points of interest in HEAs is the development of a single-phase microstructure, despite being made up of a multitude of elements (five or more) in high concentrations. As of now, the most commonly found crystal structures, which have been reported in the literature, are fcc and bcc structures. Hexagonal close-packed (hcp) HEAs, on the other hand, are less common [1].

The reason why fcc and bcc structures are preferentially formed might lie within the selection of elements. When developing a HEA, most of the time, it is the aim to end up with a single-phase material, so it is only natural to try to obey the Hume-Rothery rules as well as possible, which means that the elements should have similar atomic radii and crystal structures [1]. Furthermore, the intent oftentimes is to end up with a fcc structure, since these systems are typically more ductile when compared to other crystal structures due to the availability of planar dislocation glide on the classical slip system [15].

Oftentimes, HEAs are reported to consist of a disordered single phase solid solution, while in fact, they could be identified as intermetallic and/or ordered phases if higher resolution methods were used. The reason lies within the complex composition and interactions which might reduce the intensity of superlattice peaks in XRD [1]. Due to these circumstances an ordered phase might only be revealed by using TEM [1, 19].

2.4.3 Stability of solid solutions

For high temperature applications it is necessary that the microstructure of a given alloy does not change. This means, that it's especially important that the microstructure

does not dissociate into other phases and no precipitates or intermetallic phases are formed, even when exposed to high temperatures for a long time [20]. Even if an alloy does not show any of these signs of instability, it is not guaranteed that the present microstructure is the one corresponding to the thermodynamic equilibrium [1]. Miracle [1] writes that micro- and macroscopic gradients in compositions are a clear sign that equilibrium is not reached, that the equilibrium is hard to verify and that there is no standard approach to achieve equilibrium.

To investigate the stability, one can anneal an alloy for a long time at high temperatures, optimally at a variety of different temperatures [1]. An alternative way of testing the stability is by previously subjecting the sample to severe plastic deformation (SPD), as was performed by Schuh et al. in past research papers [21, 22].

According to a study by Miracle et al. [1], a large amount of HEA research was being done on samples in the as-cast state only. Since the as-cast state does not represent a thermodynamic equilibrium, annealing oftentimes dissociates the microstructure, meaning that the number of actual single-phase HEAs is lower than the number of reported ones.

The Cantor alloy (FeCrMnNiCo), for example, was previously thought to be a stable, single-phase material over a range of temperatures from room temperature to its melting point [23, 24]. However, recent studies with high-resolution characterization methods have found that this alloy does indeed form secondary phases under certain conditions. Pickering et al. [25] found that after an annealing at 700°C for 100h a second phase and after 1000h a third phase was formed, both of which are decorating the grain boundaries. Schuh et al. [21] found that after SPD and annealing at 450°C precipitates were formed even at annealing times as low as 5 minutes.

2.4.4 Severe plastic deformation

Severe plastic deformation is a process where the sample is subjected to very high plastic strain. This leads to the formation of a high defect density, particularly dislocations, to the formation of substructures and ultimately to the formation of an equiaxed “ultrafine” grain size or nanocrystalline structure [26]. All of these lead to an increase in nucleation sites, which increases the speed of phase transformations but also promotes the recrystallization of the microstructure [27]. All in all, the driving force for decomposition and for secondary phase formation increases a lot, which means that even alloys which seem to be stable after classic methods show signs of dissociation

[21, 22].

In addition to the destabilization of the microstructure, SPD also increases strength in alloys due to the increase in dislocation density and grain refinement, which can ultimately even lead to a nanocrystalline microstructure [28]. Furthermore, it was reported that an increase in ductility of nanostructured metals and alloys can sometimes be observed after being subjected to SPD and defined heat treatments [21, 28].

High pressure torsion

High pressure torsion (HPT) is a widely used SPD method. The principle behind HPT is as follows: a sample is deformed between two anvils which are loaded with a very high hydrostatic pressure [26, 28]. While this pressure is being applied an electric motor rotates one of the anvils with a specified rotational speed. This rotation introduces torsional shear straining. Due to the high hydrostatic forces the formation and propagation of cracks is severely inhibited, allowing for very large plastic strains [28].

2.5 The AlTi-X-NbV system

The search for HEAs with balanced mechanical properties, both at low and high temperatures, but also with a low density resulted in the development of alloys based on Al-TiNbV. It has been shown that AlTiNbV by itself has a single-phase bcc microstructure and exhibits a good compressive strength up to a temperature of 800°C [29]. Under the influence of HPT and annealing in a range between 300°C and 1000°C, this alloy forms further phases, proving that it is thermodynamic unstable in these temperature ranges [22].

An improvement of this alloy is partially based on introducing a fifth element, which is an equiatomic quinary alloy. While both, the addition of Cr [30] and Zr [19], can potentially improve the mechanical properties at various temperatures, none of the aforementioned elements promote the formation of just one solid solution [19, 30].

In this alloying system Al has a special role. Firstly, due to the high bonding strength to the other constitutive elements, the Al content is thought to severely impact the mechanical properties of the alloy, and therefore is responsible for a poor ductility at ambient temperatures [29]. And secondly, the addition of Al stabilizes the bcc structure and promotes the formation of a B2 structure [31, 32].

3 Materials and experimental methods

3.1 Selection of materials

The selection of the materials that should be investigated was the first important step in this master thesis. One condition was that the alloys must contain Ti and Al, since the aim of this work was to develop a light-weight material. Another advantage is that there is a huge foundation of knowledge about Ti and Ti alloys (especially the TNM alloy) in the department in which this work was written. Moreover, previous research papers (see Schuh et al. [22], Yurchenko et al. [19] and Stepanov et al. [29]) reported valuable results with HEAs based on Ti and Al.

In preparation for this work various alloy systems had been investigated by applying the Hume-Rothery rules and by taking the solubility of the binary systems into account. The resulting alloys should be used as first candidates and starting point for the research. They have the following chemical compositions:

- AlTiMoNbV (20 at% each) and
- AlTiMnNbV (20 at% each).

As the research on these alloys was in process and knowledge about these systems was being generated, it was evident that a successful alloy development would require the investigation of further alloy variants with slightly different and optimized chemical compositions. The following alloys were also produced and tested in this work:

- $\text{Al}_{20}\text{Ti}_{30}\text{Mn}_{10}\text{Nb}_{20}\text{V}_{20}$ and
- $\text{Al}_{20}\text{Ti}_{10}\text{Mn}_{30}\text{Nb}_{20}\text{V}_{20}$.

All of these samples were produced by GfE Metalle und Materialien GmbH, Nuremberg, Germany, in a plasma oven by remelting master alloys with a purity of 99.99% and subsequent multiple remelting to ensure chemical homogeneity. The alloys were cast onto a water-cooled copper plate and Argon was used as plasma gas.

3.2 Microstructural characterization

To produce metallographic cross-sections, all alloys were prepared in the same way. The preparation included the following steps:

1. Cut out the sample with a precision cutting machine (ATM Brilliant) using a diamond-coated cutting blade and a forward speed of 0.7 to 1.0 mm/min at a rotational speed of 3000 RPM.
2. Embed the sample in a conductive mounting resin (Struers Polyfast) using a Struers CitoPress and the recommended pre-programmed parameters for the selected mounting resin. The resin was heated for 3.5 minutes at a temperature of 180°C and a pressure of 250 bar. After this the sample was cooled for 1.5 min with cooling rate “High”.
3. Grinding of the embedded samples with a SiC grinding paper using grain size numbers of 320, 500, 800, 1000, 1200, 2000 and 4000 for 3 minutes. Each grinding step was performed under water cooling at a Struers TegraPol machine. A force of 30 to 40 N and a rotational speed of 300 RPM was used.
4. Polishing the samples with a suspension of alumina particles with a particle size of 3 μm and 1 μm for 5 minutes each using a Struers TegraPol machine using a force of 20 N and a rotational speed of 150 RPM. An oil based lubricant was used.
5. Polishing the samples with an OP-S dispersion for 5 minutes using 10 N per sample and a rotational speed of 150 RPM.
6. Ultrasonic cleaning of the samples in a bath of 2-propanol.

Samples which were analyzed by light optical microscopy were etched in a bath of *Kroll's* etching reagent. The samples were etched for a duration of 12 to 15 seconds at room temperature.

Light optical microscopy was performed with a Zeiss Axioskop microscope using bright-field imaging.

Imaging of the samples in the scanning electron microscope (SEM) were performed in the polished and cleaned state with a Zeiss EVO50 SEM using a backscattered electron (BSE) detector and an acceleration voltage of 15 kV.

3.2.1 Heat treatments

Heat treatments were primarily performed in a Carbolite RHF 1600 high-temperature oven which uses electrical heating coils as heating element. No protective gas or vacuum was used. Since the most heat treatments are specific to the alloy in question

the relevant parameters are given in the results and discussion section of this work (chapter 4).

All alloys were subjected to a homogenization heat treatment to ensure the chemical homogeneity of the samples. In the beginning, the temperatures and times from previous publications of similar alloys (see [29]) were used. The AlTiMoNbV alloy was, for example, annealed for 24 h at a temperature of 1200°C, the other alloys for the same time but at a temperature of 900°C. The samples were furnace cooled.

Selected heat treatments were performed in a dilatometer with inert atmosphere and controlled cooling rates. For these experiments a Bähr DIL 805 A/D quenching dilatometer was used. While the holding times and cooling rates were selected to achieve a desired microstructure (which can be taken from the relevant sections within chapter 4), the heating rates were selected to have a reasonably quick heating segment, i.e., the heating rates were typically 10 K/s. On both sides of the samples a thin tantalum disk was glued, using a cyanoacrylate based adhesive (super glue), to prevent reaction with the dilatometer pushrod. During heating and holding a vacuum was used to prevent oxidation at high temperatures. Cooling was performed with a stream of nitrogen gas.

3.3 Crystal structure analysis

In order to obtain the crystal structure of the present phases within the samples, X-ray diffraction (XRD) experiments were conducted. The measurements were performed with a Bruker Advance D8 X-ray diffractometer. All of the samples for XRD were prepared in the same way as the metallographic cross-sections for SEM, but were bedded out. For the experiments Cu-K α radiation was used (wavelength of 1.5406Å) which was produced by the X-ray source with an acceleration voltage of 40 kV and a current of 40 mA. The measurements were performed over 2Θ angles between 5 and 120° with an angular speed of 0.0015 to 0.003 degrees per second.

The XRD peaks, which were measured at specific Bragg angles, were analyzed to determine the crystallographic structure and the lattice parameters. As none of the alloys had published XRD data at the present time, two strategies were used, depending on types of present phases.

For diffractograms which clearly showed only a single cubic phase the peaks were at first indexed and then the lattice parameter, which corresponds to its angle via the

Bragg condition [33], was calculated for each peak:

$$2d \cdot \sin(2\phi) = n \cdot \lambda \quad (3.1)$$

Where 2ϕ is the glancing angle, d is the interplanar spacing which corresponds to the lattice parameter and the Miller index of the respective plane and λ is the wavelength of Cu-K α radiation [33].

For more complex diffractograms more effort was needed. At first the XRD data was analyzed with the software DIFFRAC.EVA from Bruker and the search function was used to find phases which match the given XRD pattern as well as possible. For this, the search was not confined to the chemical composition of the sample but rather to all transition metals and also Aluminium. For all alloys bcc and hcp phases were found most often.

The second step was to take the data from these phases (Bragg angle, intensity and Miller indices) and match these indices to the peaks of the measured diffractogram.

Finally, the lattice parameters were calculated by using Bragg's law. For hexagonal phases, however, the interplanar spacing is given by following equation [34]:

$$\frac{1}{d_{hkl}^2} = \frac{4}{3} \cdot \left(\frac{h^2 + hk + k^2}{a^2} \right) + \frac{l^2}{c^2} \quad (3.2)$$

where h , k and l are the Miller Indices of the respective plane and a and c are the hexagonal lattice parameters.

The lattice parameters were calculated by finding the values which satisfy both Eq. 3.1 and Eq. 3.2 by approximation using the mathematical software Octave and working with a maximum error of 0.001Å.

3.4 Thermal analysis

Phase transition temperatures were determined by differential scanning calorimetry (DSC) using a Setaram LabSys Evo machine. All samples were weighed in at 50 to 60 mg and all experiments were performed under Argon atmosphere while using a Al₂O₃ crucible. The heating and cooling rates of the various experiments can be found in the corresponding sections of chapter 4.

3.5 Density and hardness

3.5.1 Density

The density ρ was measured by weighing the sample and dividing the mass m by the volume V . The volume was determined by measuring the displacement of a column of water after the sample had been fully immersed.

$$\rho = \frac{m_P}{\Delta V} = \frac{m_P}{(h_2 - h_1) \cdot C} \quad (3.3)$$

Where C is the conversion factor between the volume and the height of the column of water, which was determined during a calibration experiment, and h_1 and h_2 are the heights of the water column before and after immersing the samples, respectively.

The individual measurements are not listed within the results and discussion chapter (chapter 4), but are listed in the appendix (see Tab. 5.1.)

3.5.2 Hardness

The hardness was determined with a Vickers hardness test using a Zwick testing machine, a force of $1kp = 9.81N$ and a loading time of 12 s. Forces of 5 kp and 10 kp were tested as well, but due to the large cracks at the corners of the testing imprint the measurements were not viable.

The diameters of the hardness imprints were measured with the aid of the software Stream Motion from Olympus. The hardness values corresponding to the measured dimensions of the imprint were taken from a HV1 hardness table. The hardness was calculated as an average of five measurements for each sample.

3.6 Severe plastic deformation

Some samples were subject to SPD by means of HPT. HPT was performed at the Erich Schmidt Institute of Materials Science, Leoben, in a compression testing machine with a pressure of 7.6 GPa and a rotational speed of 0.2 RPM for a total of 5 revolutions.

The samples were disk shaped with a thickness of 1 mm, a diameter of 8 mm and were produced by electrical discharge machining.

As a result of the shape of the samples, the degree of deformation is dependent on

the position within the disk, specifically on the radial distance from the center. Given a radial distance of r , a sample thickness t and the number of revolutions n the shear strain γ can be calculated by:

$$\gamma = \frac{2\pi r}{t} \cdot n \quad (3.4)$$

To extract the most information from the deformed area, samples were taken from the disk 1.5 mm off center and mounted in such a way as to obtain the viewing direction as pictured in Fig. 3.1.

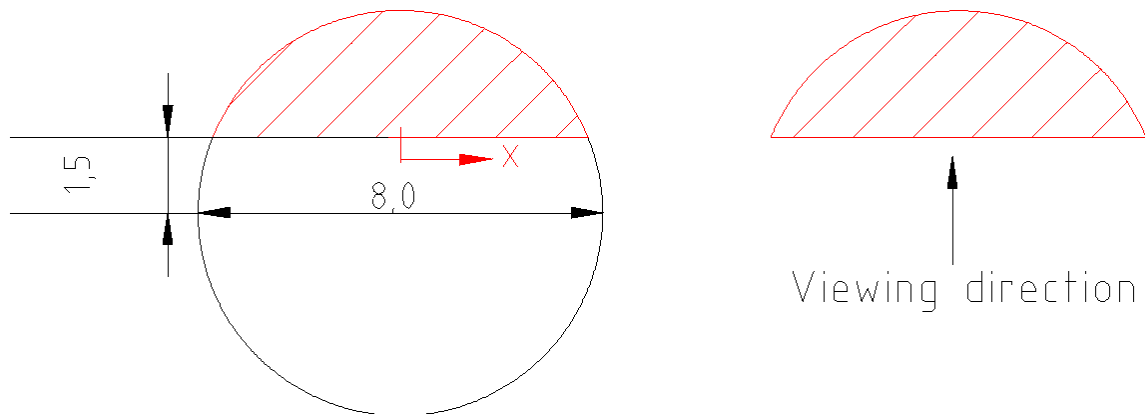


Figure 3.1: Position of the sample as part of the HPT disk and viewing direction used for metallography.

4 Results and discussion

4.1 AlTiMoNbV

4.1.1 Microstructure and stability

The as-cast microstructure of this alloy shows the presence of a single phase and a distribution of fine impurities, as can be seen in Fig. 4.1a. What can also be seen is that the microstructure is largely inhomogeneous, which stems from segregations formed during the casting process.

After a 1200°C heat treatment for 24 hours the casting inhomogeneities dissolved and a homogeneous microstructure was observed but no changes of the contaminations occurred (see Fig. 4.1b). The sample was furnace-cooled as part of the diffusion heat treatment, which corresponds to a time of cooling to room temperature over several hours. As the sample was cooled down very slowly and due to the fact that no new phases appeared, it is plausible that the single-phase microstructure corresponds to the equilibrium state.

Despite the results from the diffusion heat treatment, the sample was aged at 750°C for 24 h, following air cooling, to validate the thermal stability of the microstructure at this temperature. No changes to the overall microstructure were observed (see Fig. 4.1c) for this temperature as well. With the previous results in mind, this alloy seems to have proven itself as thermally stable over a wide range of temperatures, at least down to temperatures where diffusion kinetics start to become too slow.

Additionally, the alloy was heated up to 1300°C in a dilatometer and quenched with a rate of 2400 K/s. However, no change in microstructure or hardness could be observed, both of which was expected when the previous results are considered.

EDX measurements concluded that the impurities are Ti- and N-rich (see Fig. 4.1a,d) and are likely to be TiN contaminations formed during sample production. The measured chemical composition of the alloy can be found in Tab. 4.1.

Table 4.1: Chemical compositions in atomic percent of the AlTiMnNbV alloy as compared to the nominal composition.

	Al	Ti	Mo	Nb	V
Nominal composition	20	20	20	20	20
Measured	20.41	20.23	19.93	20.43	19.01

4.1.2 Crystal structure analysis

XRD measurements were performed and verified the present phase to be a bcc structure with a lattice parameter of 3.17 Å, in both the as-cast and homogenized state. The respective reflections and the corresponding crystallographic indices can be taken from Fig. 4.2.

Following the procedure, as described in the experimental section, the lattice constants can be calculated for each peak, see Tab. 4.2 for the results.

Table 4.2: Calculation of the lattice parameter a corresponding to the different XRD peaks present in Fig. 4.2.

Plane [hkl]	2Θ	$\frac{\sin^2(\Theta)}{h^2+k^2+l^2}$	a [Å]
[110]	40.26	0.0592	3.16
[200]	58.01	0.0588	3.18
[211]	73.00	0.059	3.17
[220]	86.87	0.0591	3.17
[310]	100.51	0.0591	3.17

4.1.3 Density and hardness

The density was determined to be 5.5 g/cm³, which is within the expected range.

The hardness was measured for a sample in the as-cast state and a sample which was heated to 1300°C and quenched. The measured hardness values are 515 ± 16 HV1 and 481 ± 26 HV1, respectively. The decrease in hardness in the latter was not further investigated, but might be attributed to grain growth effects.

4.1.4 Thermal analysis

DSC was employed to investigate existing phase transition temperatures. To this end the alloy was subjected to two different experiments. A heating ramp from 30°C to 1600°C with a heating rate of 30 K/min was conducted, followed by a loop of three subsequent cycles with 20, 15 and 10 K/min for both the heating and cooling rate. No peaks were observed which could indicate the presence of a phase transition.

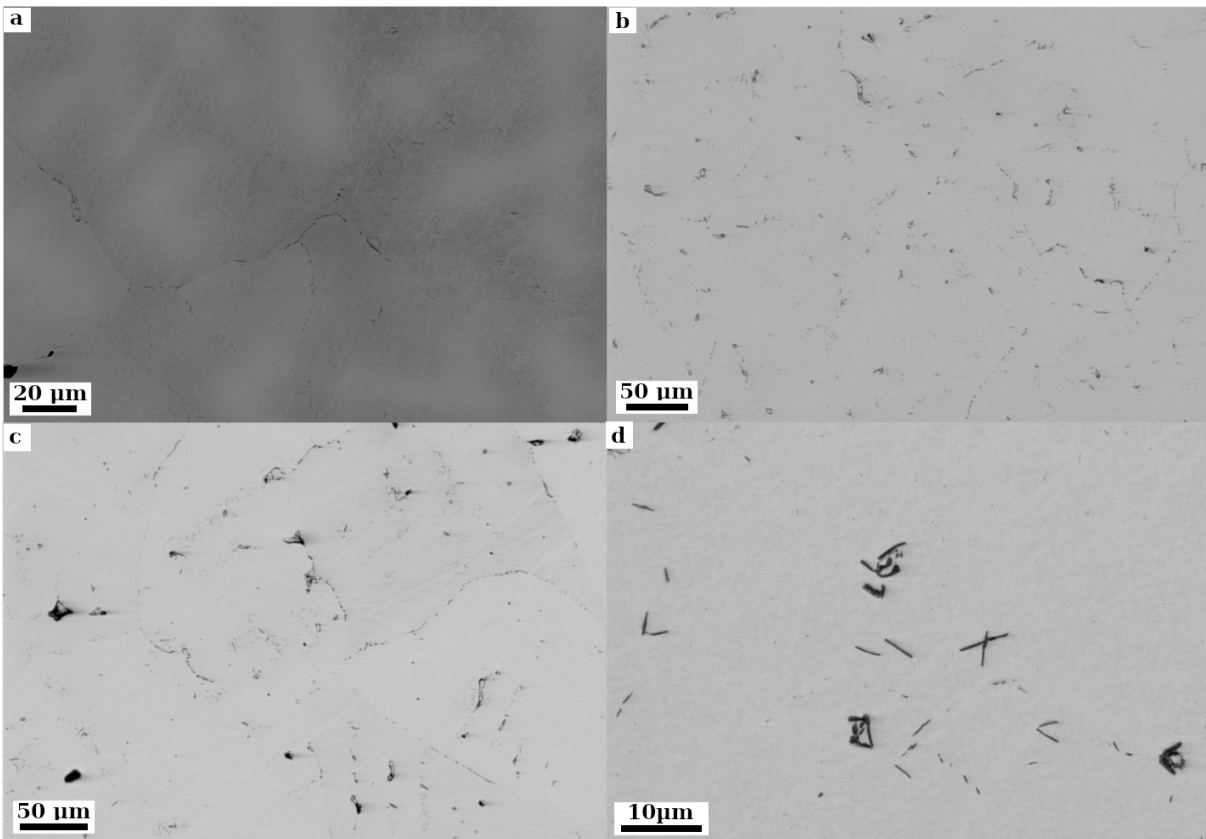


Figure 4.1: SEM-BSE images of AlTiMoNbV in the a) as-cast, b) homogenized and c) aged (750°C/24 h) state. d) Detail of the contamination in the aged condition.

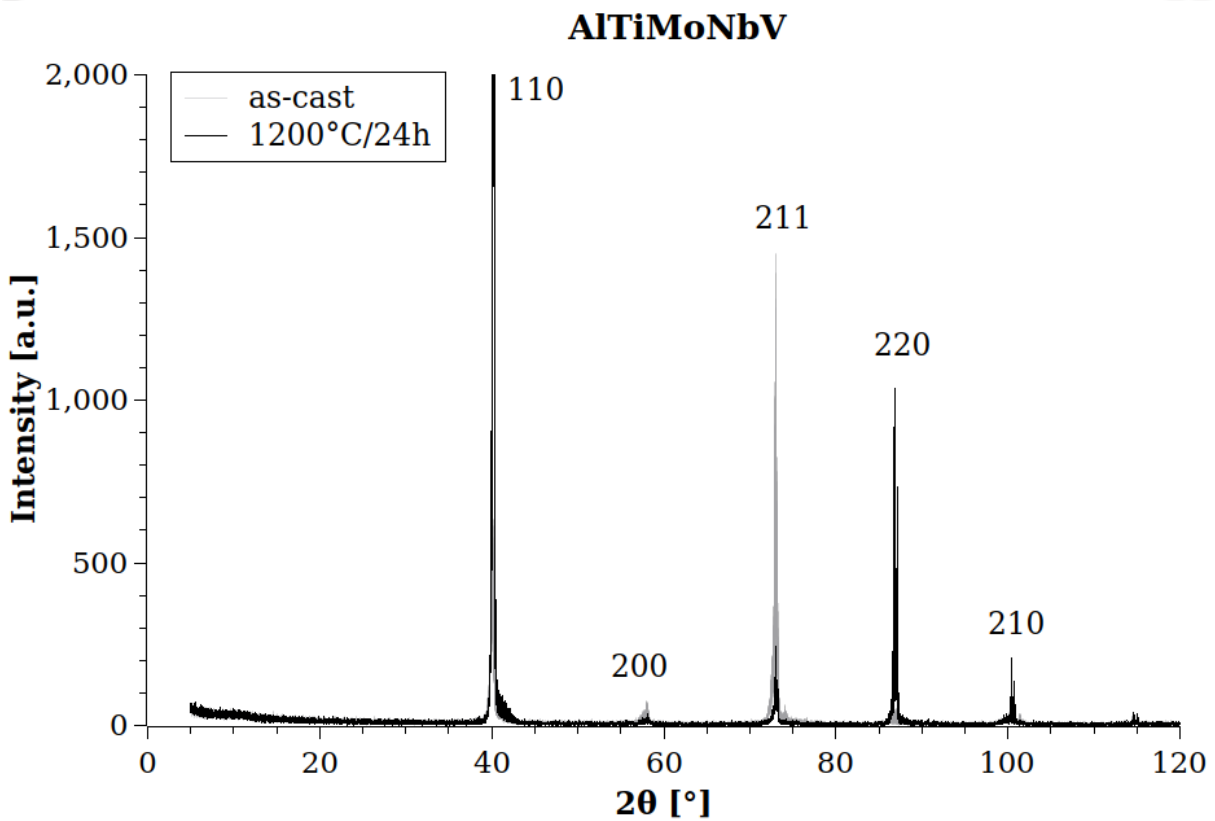


Figure 4.2: XRD pattern of AlTiMoNbV in the as-cast and homogenized state.

4.1.5 Severe plastic deformation

This alloy was furthermore subjected to SPD by means of HPT. The aim was to introduce a very high density of defects to increase the total energy of the sample and, should the bcc solid solution not be the stable phase, promote the decomposition of the solid solution into a more equilibrium-like state. The samples were subjected to a pressure of 7.6 GPa and sheared for 5 revolutions at a speed of 0.2 RPM. The corresponding torque-shear diagram can be found in the appendix (Fig. 5.7).

After HPT one sample was prepared in the as-deformed state, while another sample was at first annealed at 450°C for one hour and subsequently air-cooled. The hardness was measured in 10 different sites along a straight line from the center to the outer radius, as described in the experimental section. In both cases, a large increase in hardness was observed, compared to the initial hardness of 517 HV1 (see Fig. 4.3). For the as-deformed sample, the hardness clearly increases linearly with increasing strain, exhibiting hardness values in the vicinity of 700 HV1. The annealed sample showed no clear correlation between hardness and strain, but overall the hardness was even higher, reaching values close to 760 HV1.

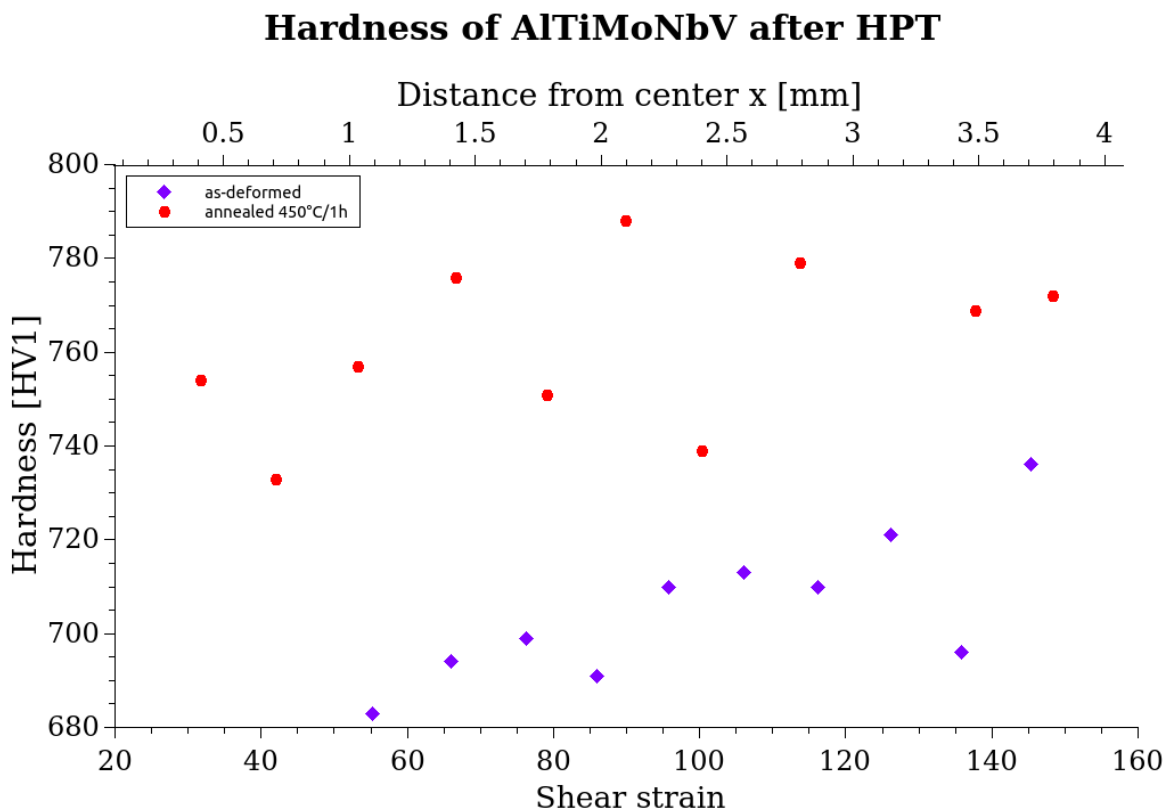


Figure 4.3: Hardness of the AlTiMoNbV alloy as function of the shear strain for the as-deformed and annealed state.

The SEM image of the as-deformed and the annealed sample (see Fig. 4.4a and b, respectively) show the effect of HPT as a clear grain orientation within the microstructure is visible in both cases. The annealed sample seems to exhibit a finer structure than the as-deformed one, but other than that no significant differences are observed.

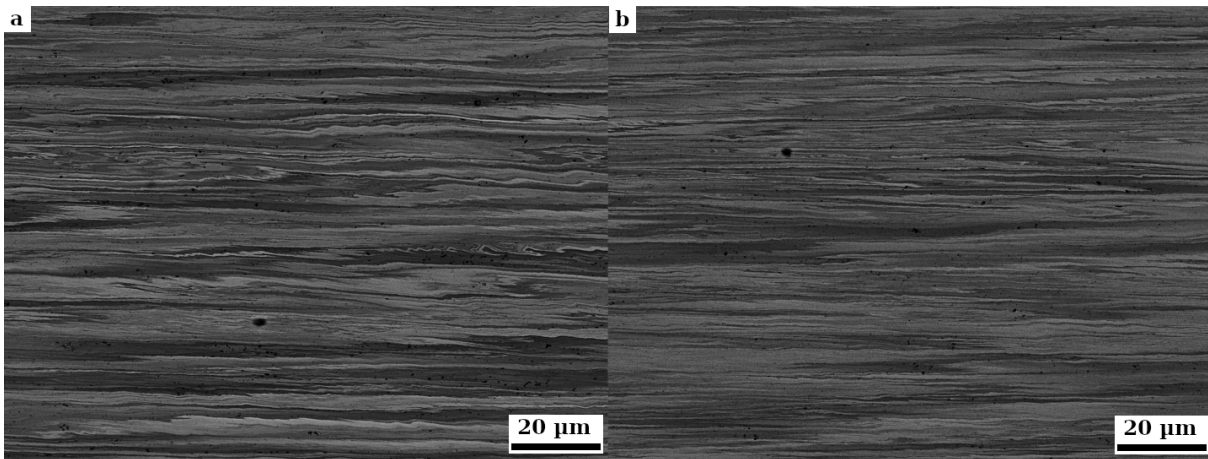


Figure 4.4: SEM-BSE image of AlTiMoNbV a) after HPT, b) after HPT and annealing at 450°C for 1 hour, followed by air-cooling.

4.1.6 Summary

In terms of microstructure and thermal stability, this alloy shows great promise to be a viable high-entropy alloy for high-temperature applications. The microstructure consists of a single bcc phase and no phase transitions or decomposition effects could be observed up to a temperature of 1200°C. Furthermore, even after being subjected to HPT, the alloy did neither decompose into different phases nor any precipitates are formed.

One problem, which was experienced with this particular alloy, was that it was contaminated with titanium nitrides, which were present both within the grains and along grain boundaries. Since these contaminations were already present in the as-cast state, they were probably introduced during the production process. If in further research the mechanical properties of this alloy will be tested this issue would need to be solved by choosing a different and cleaner production method.

The next characterization step with this alloy could be, that even higher annealing temperatures are used for HPT samples and that methods with higher resolution, such as transmission electron microscopy (TEM) and atom probe tomography (APT) are employed to find any very fine secondary phases.

4.2 AlTiMnNbV

4.2.1 Microstructure and stability

In the as-cast state this alloy shows a two-phase microstructure, consisting of “star-shaped” clusters of a secondary phase within the matrix phase (see Fig. 4.5 a). After being heat treated at 900°C for 24 h and air-cooled, the shape of the secondary phase changes to long-stretched grains as seen in Fig. 4.5 b.

After a heat treatment in the dilatometer, consisting of being held at 1200°C for 15 min and then rapidly cooled with 2400 K/s, the volume fraction of the secondary phase is drastically reduced as can be seen in Fig. 4.5d. It is possible that the secondary phase could completely diminish if the holding time is extended, but due to the high-vapor pressure of Mn at this temperature and the presence of a vacuum during heating and holding as well as the risk of contaminating the furnace, this consideration was not pursued further. However, the experiment was repeated at a temperature of 900°C and a holding time of 2 hours, but no change in microstructure in comparison to the initial state could be observed, which suggests that the solvus temperature must lie between 900°C and 1200°C.

Quantitative EDX measurements of a sample in the homogenized state were performed, the investigated phases are indicated in Fig. 4.5c and their chemical composition can be taken from Tab. 4.3. It was found that both phases are similar in their concentrations of Al, Nb and V and complementary in their Ti and Mn concentrations. This fact gave rise to the idea in trying to create a single-phase high-entropy alloy with chemical compositions close to the phases analyzed in Tab. 4.3. Those new alloys then have the nominal compositions of $\text{Al}_{20}\text{Ti}_{30}\text{Mn}_{10}\text{Nb}_{20}\text{V}_{20}$ and $\text{Al}_{20}\text{Ti}_{10}\text{Mn}_{30}\text{Nb}_{20}\text{V}_{20}$.

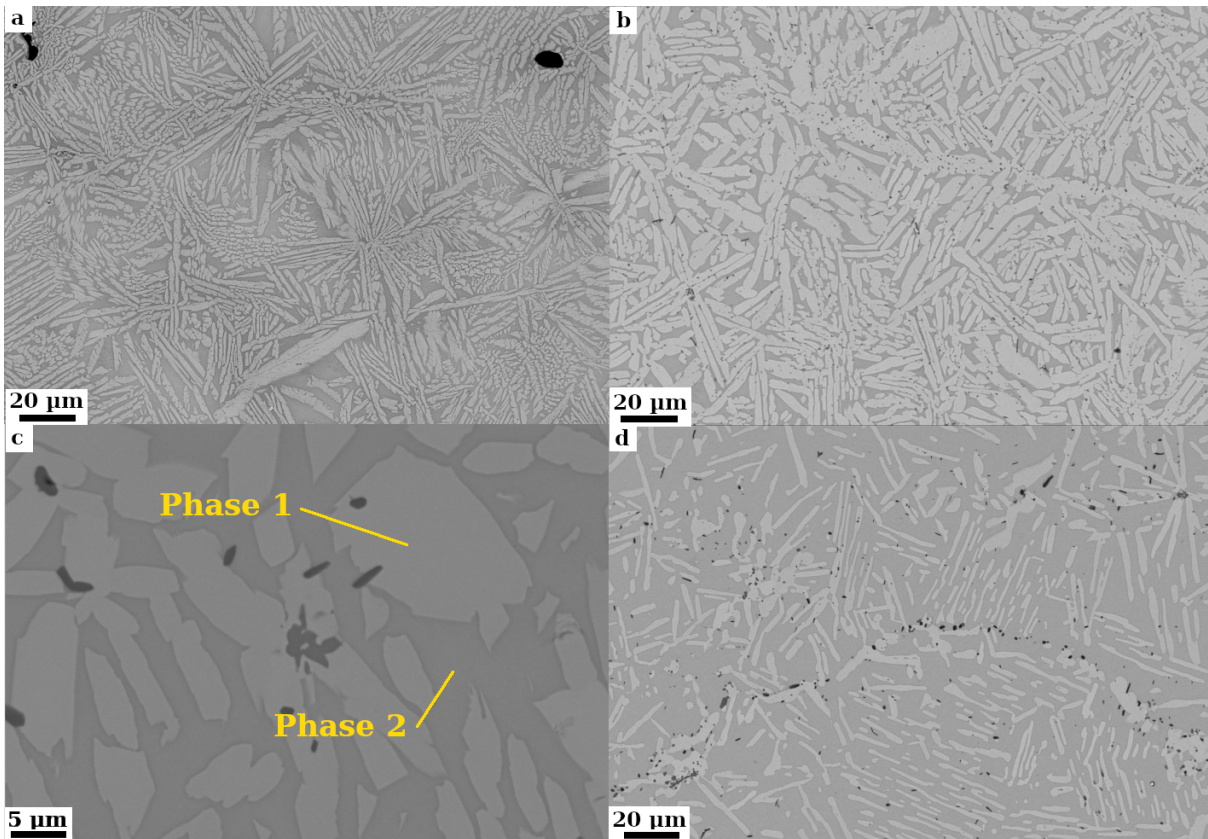


Figure 4.5: SEM-BSE images of the AlTiMnNbV alloy in the a) as-cast, b), c) homogenized, and d) heated and quenched state.

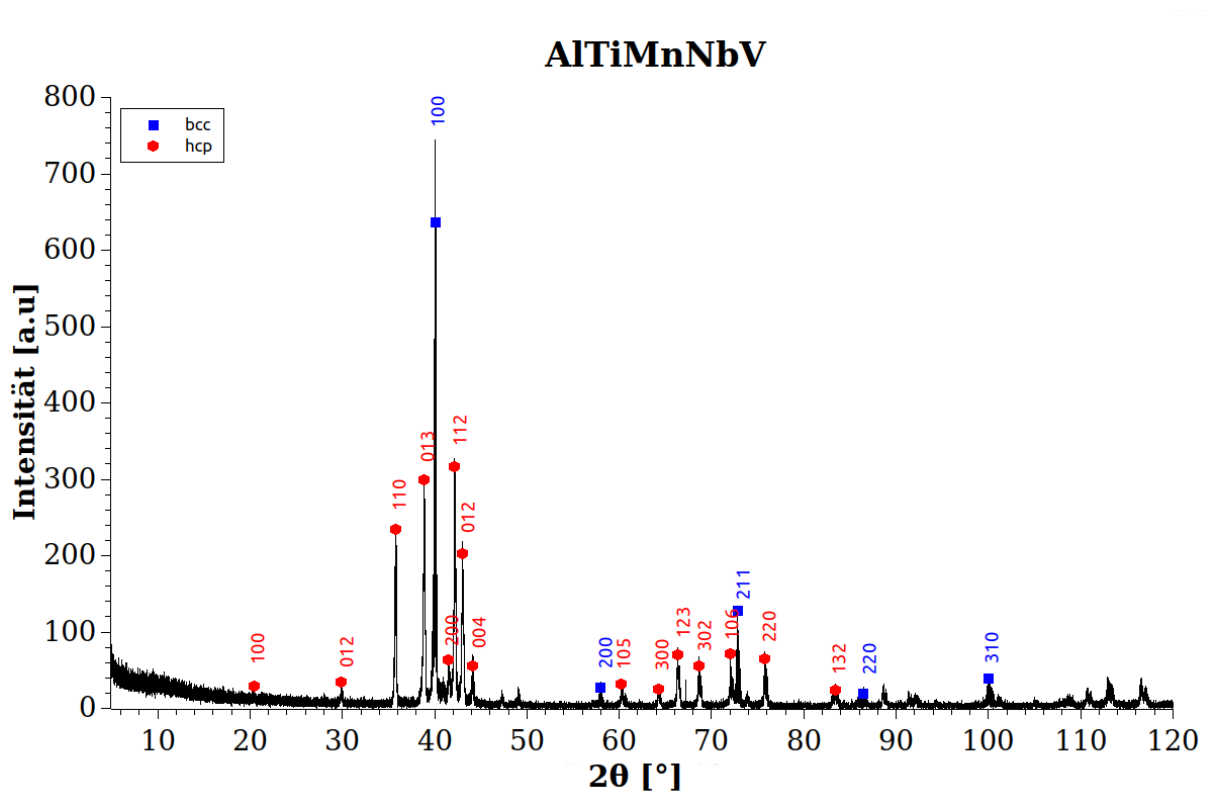


Figure 4.6: Diffraction patterns of the AlTiMnNbV alloy in the homogenized state.

Table 4.3: Chemical compositions in atomic percent of the AlTiMnNbV alloy as well as the present phases. The labeling of the phases corresponds to Fig. 4.5c

	Al	Ti	Mn	Nb	V
Nominal composition	20	20	20	20	20
Measured	20.80	20.57	18.53	20.67	19.44
Phase 1	18.2	12.5	28.6	19.4	16.6
Phase 2	20.1	25.1	11.2	19.4	22.5

4.2.2 Crystal structure analysis

XRD measurements of the as-cast state showed the presence of a bcc phase with a lattice parameter of 3.18 Å and a hcp phase with lattice parameters $a=5.01$ Å and $c=8.19$ Å. The respective reflections and the corresponding crystallographic indices can be taken from Fig. 4.6.

Following the procedure as described in the experimental section, the lattice constants for each plane of the bcc phase are determined as summarized in Tab. 4.4

Table 4.4: Calculation of the lattice parameter a for the bcc phase corresponding to the peaks shown in Fig. 4.6.

Plane [hkl]	2Θ	$\frac{\sin^2(\Theta)}{h^2+k^2+l^2}$	a [Å]
[110]	39.99	0.0585	3.19
[200]	57.85	0.0585	3.18
[211]	72.66	0.0585	3.18
[220]	86.55	0.0587	3.18
[310]	99.85	0.0586	3.18

In order to show the validity of the lattice constants for the hcp phase the theoretical interplanar distance d_{hkl}^{th} [Å] is calculated, which corresponds to the given plane (given by Eq. 3.1) and then compared to the interplanar distance d_{hkl}^{exp} [Å] obtained from experimental data. The interplanar distance is evaluated by solving Eq. 3.2.

Plane [hkl]	2Θ	d_{hkl}^{th} [Å]	d_{hkl}^{exp} [Å]
[110]	35.77	2.505	2.507
[103]	38.88	2.311	2.313
[004]	44.12	2.048	2.050
[213]	67.08	1.406	1.394
[220]	75.80	1.253	1.254

Table 4.5: Comparison of the theoretical interplanar distance d_{hkl}^{th} acquired by solving Bragg's equation to the interplanar distance d_{hkl}^{exp} acquired by evaluation of the experimental data (see Fig. 4.6).

Considering the experimental error, the interplanar distances are close enough to con-

sider the obtained results valid.

4.2.3 Density and hardness

The density of this alloy has been determined to be 5.0 g/cm^3 . The hardness was found to be $740 \pm 7 \text{ HV1}$. The hardness is thought to be influenced by the presence of the second phase. Future nanoindentation experiments could be used to verify or disprove this consideration.

4.2.4 Thermal analysis

In order to find possible phase transition temperatures DSC was employed. The samples were heated and cooled with rates of 20, 15 and 10 K/min up to temperatures of 1200°C . By extrapolating the temperatures to a cooling rate of 0 K/min a solvus temperature of 1013°C was found.

In addition, another experiment was performed where the sample was heated to a temperature of 1600°C with a rate of 40 K/min and cooled with a rate of 20 K/min. The sample melted in the crucible and the corresponding endothermic peak in the DSC was found to occur at a temperature of 1275°C .

The DSC measurements can be found in the appendix, refer to Fig. 5.1 and 5.2.

4.2.5 Summary

This alloy is a two-phase material consisting of a hcp phase and a bcc phase at room temperature. It was not possible to transform this alloy into a single solid solution. Although it could be shown that the amount of hcp phase could be significantly reduced at higher temperatures, a even higher temperature for heat treatment or longer annealing time did not seem reasonable due to the high vapor-pressure of Mn and the possible contamination of the vacuum furnace.

Despite being an unpromising alloy itself, it, however, was the basis for further alloy development, as the chemical compositions of the two phases were close enough to a high-entropy like alloy to be considered as new alloys themselves.

4.3 Al₂₀Ti₃₀Mn₁₀Nb₂₀V₂₀

4.3.1 Microstructure and stability

In the as-cast state, a very homogeneous single-phase material with well distinguishable grains, as seen in Fig. 4.7a, could be observed in the SEM. The diffusion heat treatment of this alloy was done at 900°C over a span of 24 hours and lead to a decomposition of the single-phase material into two phases. A matrix phase and a secondary phase was found along the grain boundaries and within the grain, together with small Al, Ti and Nb rich precipitates, as shown in Fig. 4.7b. An aging of this alloy at 750°C for 24 h in the decomposed heat treated state lead to a coarsening of the light contrasted phase which can be seen in Fig. 4.7c.

To investigate the thermal stability of the single-phase microstructure, two separate as-cast samples were subjected to heat treatments at 600°C and 750°C for 24 hours. After the heat treatment, the 600°C sample shows a microstructure with a thin layer of a secondary phase along the grain boundaries of a single phase, see Fig. 4.7e. The sample aged at 750°C exhibits precipitation of a secondary phase within the matrix phase in a repeating geometrical pattern (see Fig. 4.7f), suggesting a crystallographic orientation relationship between the matrix and precipitates.

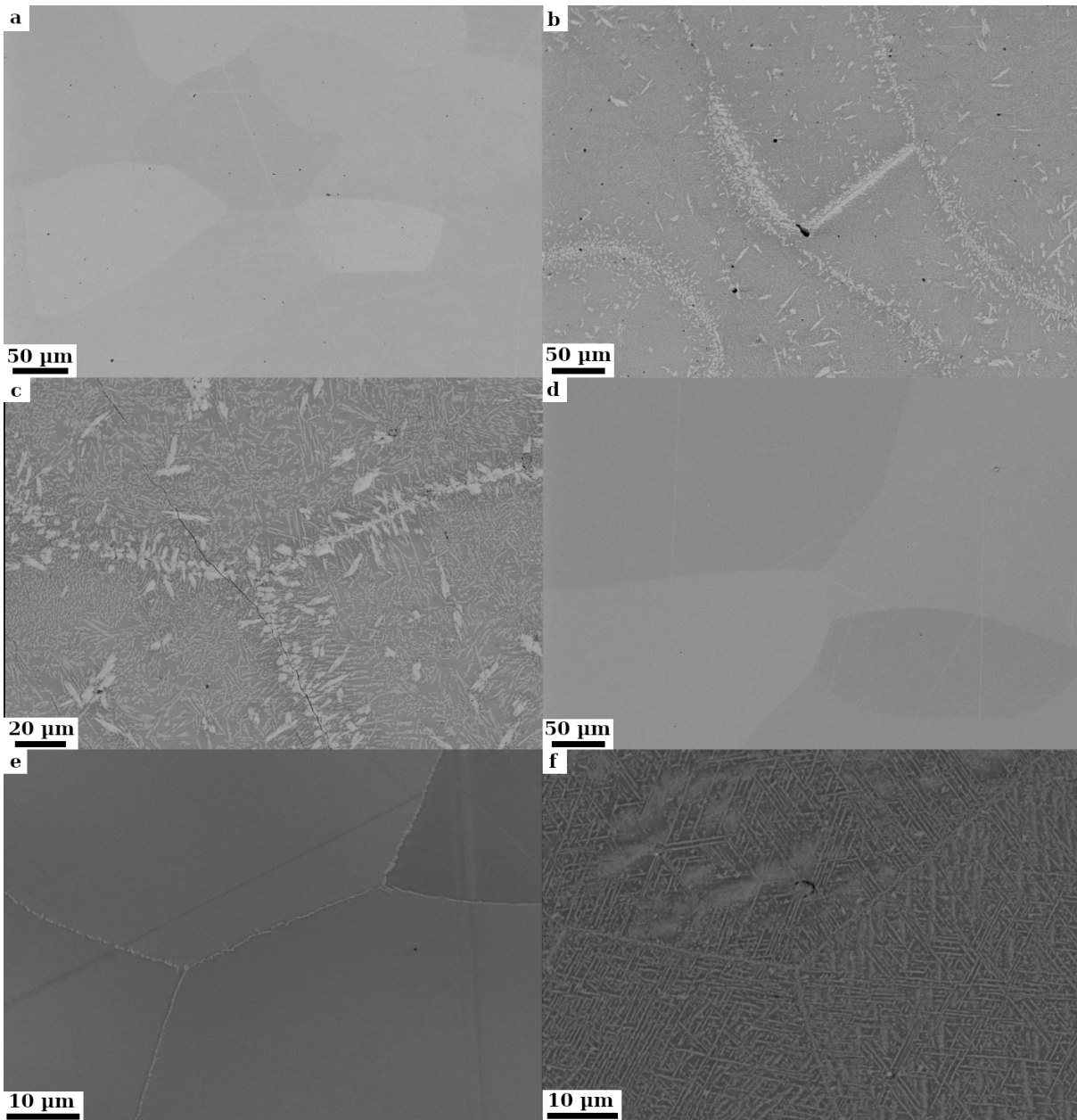


Figure 4.7: SEM-BSE images of $\text{Al}_{20}\text{Ti}_{30}\text{Mn}_{10}\text{Nb}_{20}\text{V}_{20}$ in the following states: a) as-cast, b) homogenized, c) aged (750°C after homogenization), d) heated and quenched, and e) and f) aged (without homogenization, 600°C and 750°C , respectively).

Furthermore the alloy was annealed for 100 h at a temperature of 900°C . For this, a sample was used which was homogenized at 900°C , as previously described. As can be seen in the SEM image (Fig. 4.8b), many intragranular grains of the secondary needle-like phase have grown in size. Also, and more importantly, a third phase can be observed. After this heat treatment it seems that the small precipitates are of a different phase than the larger ones, as judged by the SEM image. While not part of this thesis, further research should clarify the type and composition of this phase.

EDX measurements were performed on the annealed, decomposed state (refer to

Fig. 4.8a). These measurements show that the stable state microstructure consists of phases which greatly differ in their compositions. As the variable in this thesis and for this alloy is the Mn and Ti content, the phases are addressed as Ti-rich and Mn-rich phases. For the exact composition refer to Tab. 4.6.

Table 4.6: Chemical compositions in atomic percent of the $\text{Al}_{20}\text{Ti}_{30}\text{Mn}_{10}\text{Nb}_{20}\text{V}_{20}$ alloy and the present phases. The labeling of the phases corresponds to Fig. 4.8a

	Al	Ti	Mn	Nb	V
Nominal composition	20	30	10	20	20
Measured	20.31	30.15	9.98	20.38	19.17
Phase 1	19.15	21.54	17.03	28.38	13.91
Phase 2	21.68	34.17	6.76	19.19	18.2

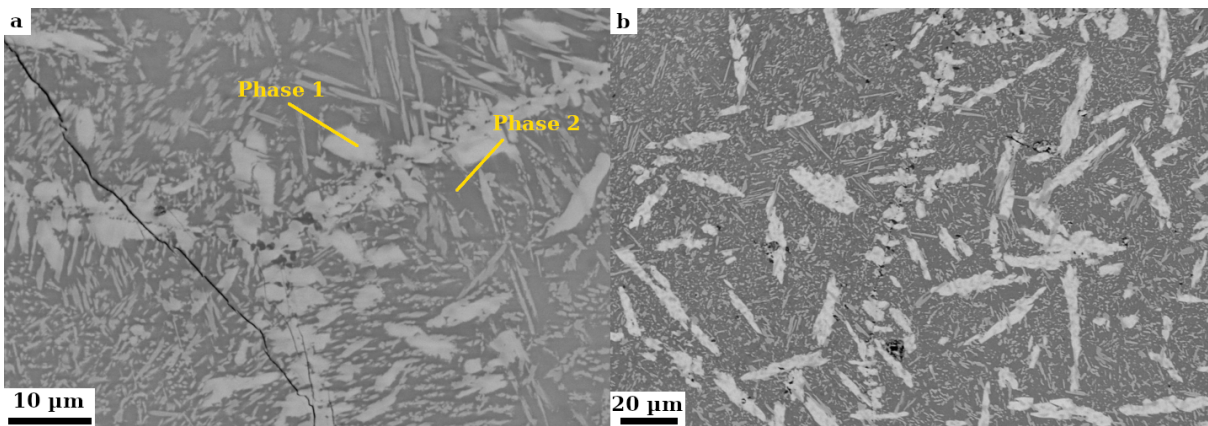


Figure 4.8: Microstructure of $\text{Al}_{20}\text{Ti}_{30}\text{Mn}_{10}\text{Nb}_{20}\text{V}_{20}$ a) after 24 h at 900°C and 24 h at 750°C and b) after 100 h at 900°C.

4.3.2 Thermal analysis

DSC measurements were performed in order to find the solvus temperature of the alloy, above which a solid solution is obtained. For this, the sample was heated to 1300°C and subsequently cooled to 100°C for three times at three different rates of 20, 15 and 10 K/min. After extrapolating to a rate of 0 K/min a solvus temperature of 1006°C was obtained. During the experiments the maximum temperature of the DSC of 1600°C was reached without melting the alloy. The corresponding DSC measurements can be found in the appendix (see Fig. 5.3 and 5.4).

4.3.3 Microstructural evolution

The microstructures after the aforementioned 24 h heat treatments at 600°C and 750°C suggest that there is a tendency for the solid solution to decompose into a two-phase microstructure, but also that 24 h is not a long enough annealing time, when coming from the solid solution, for the microstructure to change to the state as seen in Fig. 4.7c, either suggesting slow diffusion behavior or a low driving force, which might stem from a only small change in Gibbs free energy when changing from the solid solution to a decomposed state.

In an attempt to revert the decomposed sample back to a single-phase microstructure, the sample was heated to 1300°C within a dilatometer, held at this temperature for 1 hour and then quenched with 2400 K/s. The SEM picture of the sample after this procedure shows a single-phase microstructure as seen in Fig. 4.7d.

Taking this idea further, the question arises if it might be possible to obtain a solid solution if the sample is only air-cooled from its terminal temperature of 1300°C. This is an important question, since air cooling is almost always a possibility in any given setting. To investigate this matter, a sample was heated up to a temperature of 1300°C in a dilatometer and cooled with a rate of 10 K/s, to simulate the cooling rate in air.

When investigating the microstructure (see Fig. 4.9), it can be seen that a single-phase microstructure could indeed be achieved, but also that there is a strong presence of chemical inhomogeneity as indicated by the clusters of darker and lighter contrasts within the grain. Taking this result into account, the conclusion is that air quenching is not fast enough to result in the desired homogeneous single-phase microstructure (compare with Fig. 4.7a or d).

4.3.4 Crystal structure analysis

XRD measurements (see Fig. 4.10) show, that the as-cast state is made up of a single bcc phase with a lattice parameter of 3.16 Å. However, an additional, very small peak can be found at an angle of 28.24°. This peak corresponds to a reflection of the [100] plane, a forbidden reflection according to the extinction rules for a disordered bcc phase, indicating a superlattice reflection and the presence of an ordered B2 phase. A selection of relevant planes and their reflection angles can be taken from Tab. 4.7.

The decomposed sample homogenized at 900°C consists of a B2 phase with a lattice parameter of 3.18 Å and a hcp phase with lattice parameters of $a=5.01$ Å and $c = 8.19$

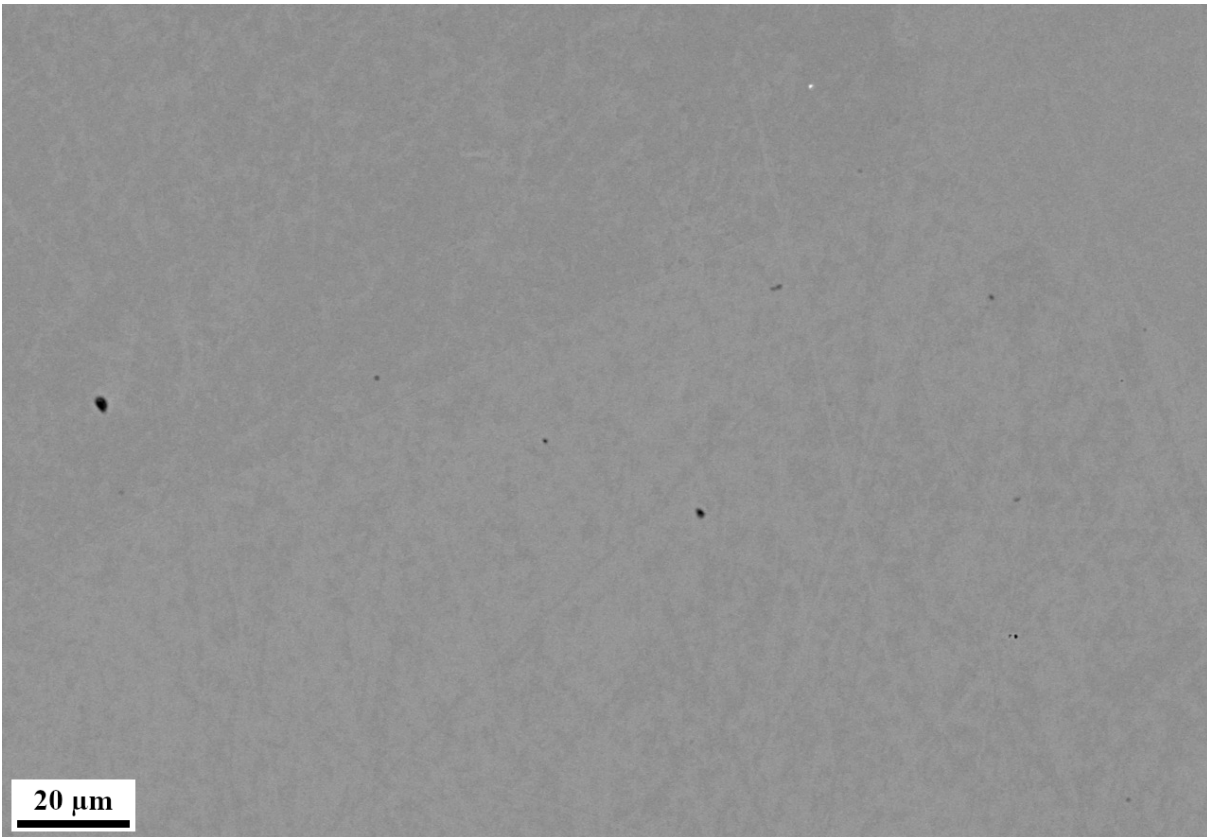


Figure 4.9: Microstructure of $\text{Al}_{20}\text{Ti}_{30}\text{Mn}_{10}\text{Nb}_{20}\text{V}_{20}$ after simulated air-quenching from 1300°C .

\AA , as calculated from the XRD diffractogram shown in Fig. 4.11. For this sample, no superlattice reflection of the B2 phase could be found, or it is not clearly distinguishable from the measured background noise.

Analogous to AlTiMnNbV a comparison of interplanar distances, for the hexagonal phase, is shown in Tab. 4.8 to show the validity of the experiment. The matching of the interplanar distances can be considered good enough, within the experimental error.

The sample annealed at 750°C was subjected to XRD measurements as well, but other than the same B2 phase no further structures could be found. This, however, might be

Table 4.7: Calculation of the lattice parameter for a B2 phase a in the as-cast state corresponding to its XRD peaks.

Plane [hkl]	2Θ	$\frac{\sin^2(\Theta)}{h^2+k^2+l^2}$	a [\AA]
[110]	40.31	0.0594	3.16
[200]	58.40	0.0595	3.16
[211]	73.38	0.0595	3.16
[220]	87.22	0.0595	3.16
[310]	101.00	0.0595	3.16
[100] (superlattice)	28.24	0.0595	3.16

Table 4.8: Comparison to the theoretical interplanar distance d_{hkl}^{th} acquired by solving Bragg's equation to the interplanar distance acquired by approximation of the lattice constants d_{hkl}^{exp} .

Plane [hkl]	2Θ	d_{hkl}^{th} [Å]	d_{hkl}^{exp} [Å]
[110]	35.91	2.505	2.498
[103]	38.94	2.311	2.310
[004]	44.18	2.048	2.048
[213]	66.65	1.406	1.402
[106]	72.68	1.302	1.300

due to the fact that the precipitates are too small and could not be resolved by XRD. The corresponding diffractogram can be found in the appendix, refer to Fig. 5.6.

To clarify the question which phase seen in the SEM images corresponds to either the hcp or B2 phase two considerations must be addressed:

1. The phase closer to the nominal composition is the phase which transforms into the solid solution at high temperatures, which is B2.
2. During decomposition, the nucleation starts at the grain boundaries, meaning that the grain boundary phase is not the high temperature phase.

Taking the results of the quantitative EDX measurements and the microstructural evolution into account it is clear that the darker phase must be the B2 phase, while the light contrasted phase represents the hcp phase.

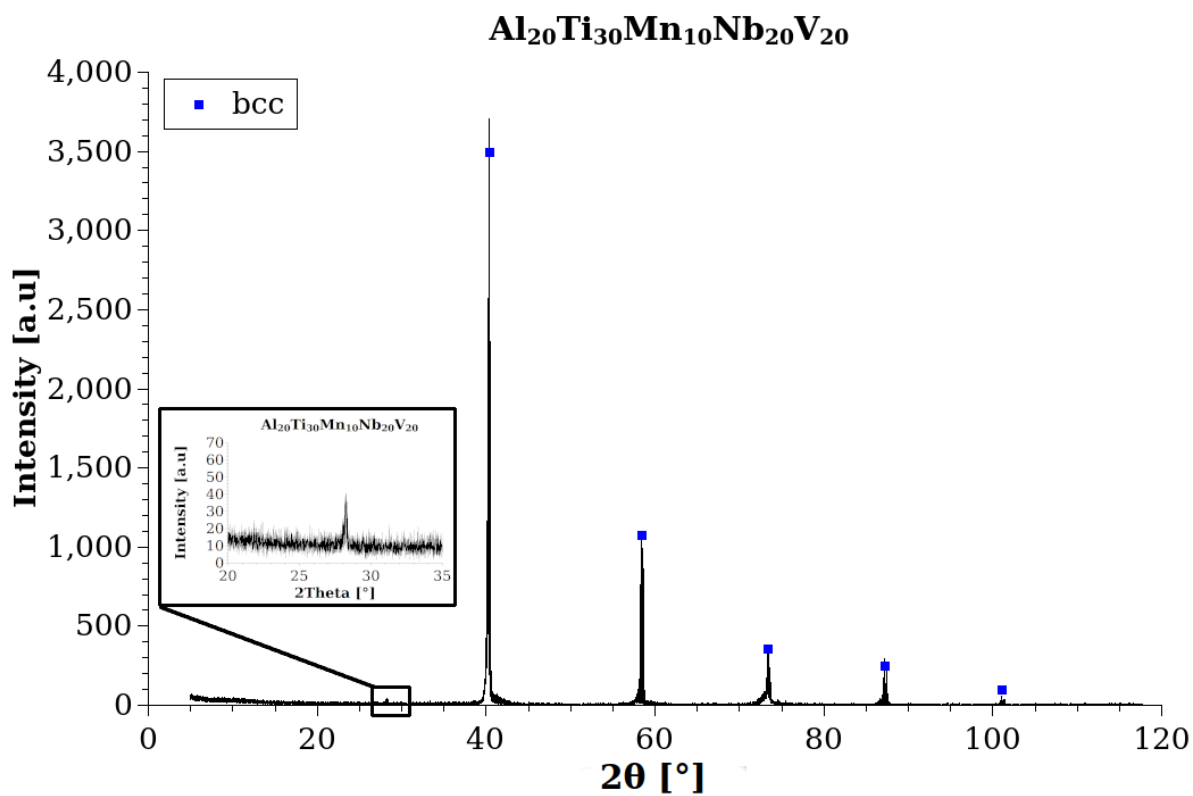


Figure 4.10: XRD diffractogram of the Al₂₀Ti₃₀Mn₁₀Nb₂₀V₂₀ alloy in the as-cast state.

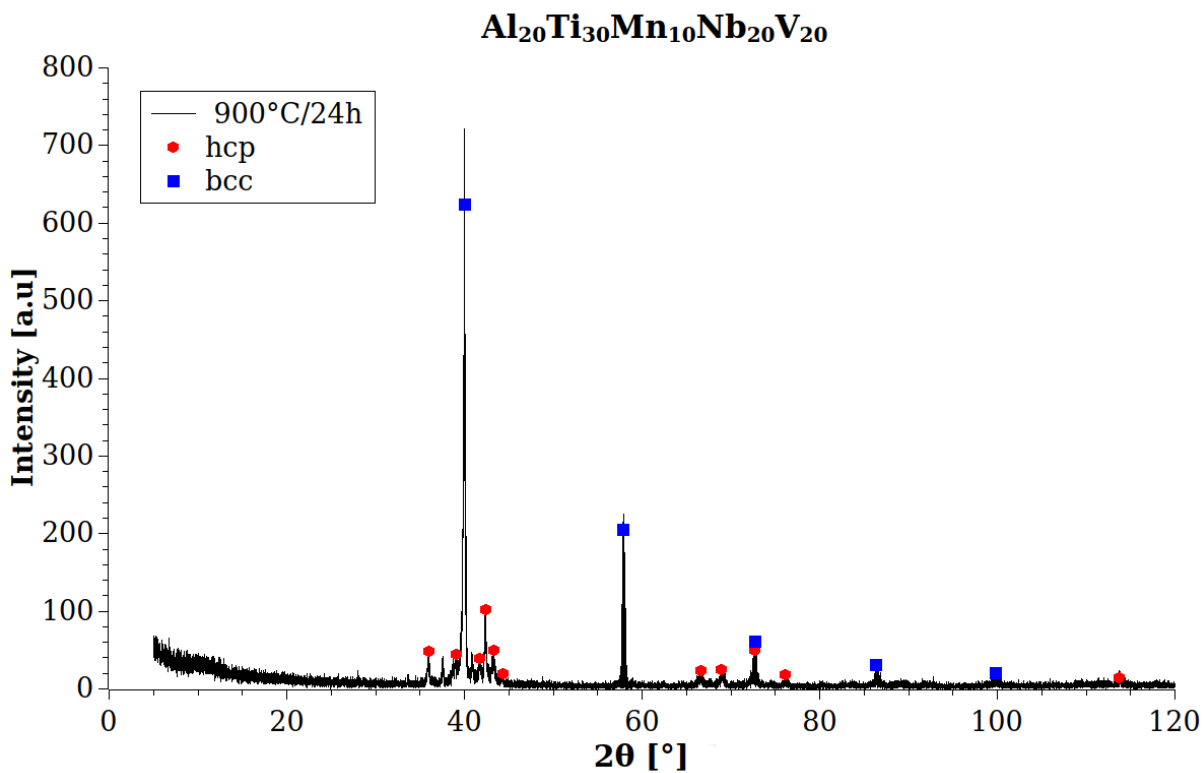


Figure 4.11: XRD diffractogram of the Al₂₀Ti₃₀Mn₁₀Nb₂₀V₂₀ alloy in the homogenized state.

4.3.5 Density and hardness

The density of this alloy was found to be 5.3 g/cm^3 at room temperature, exhibiting a hardness of $474 \pm 14 \text{ HV1}$.

Hardness tests were also performed on the various microstructural states of this alloy. As compiled in Tab. 4.9, the sample aged at 750°C does not only show higher hardness, but might also show better resistance against cracking. This can be concluded when the lines seen in Fig. 4.12 are considered as cracks.

Table 4.9: Hardness (HV1) of the $\text{Al}_{20}\text{Ti}_{30}\text{Mn}_{10}\text{Nb}_{20}\text{V}_{20}$ alloy showing different states.

	Hardness (HV1)
as-cast	474 ± 14
annealed 600°C	491 ± 25
annealed 750°C	670 ± 34
heated and quenched	494 ± 4

4.3.6 Severe plastic deformation

The alloy was subjected to HPT as well. At this point it was already known that this alloy decomposes at higher temperatures, so the aim here was to find out if the energy introduced by HPT is sufficient enough to cause a decomposition at a lower than the previously measured temperature, maybe even at room temperature. Additionally, the increased driving force caused by this procedure could lead to the formation of additional phases such as precipitates. The samples were, as described before, subjected to a pressure of 7.6 GPa and sheared for 5 revolutions at a speed of 0.2 RPM. The corresponding torque-shear diagram can be found in the appendix (Fig. 5.8).

Again, one sample was prepared in the as-deformed state, while another sample was at first annealed at 450°C for 1 hour and subsequently air-cooled. In both cases a large increase in hardness was observed, when compared to the initial hardness of 474 HV1 (see Fig. 4.13). For the as-deformed sample, the hardness increases linearly, but only slightly, with increasing strain, exhibiting hardness values of about 650 HV1 . The annealed sample showed no clear correlation between hardness and strain, but overall a very large increase in hardness was observed, reaching values of about 800 HV1 .

In both the as-deformed and annealed state, this alloy shows a very fine microstructure after HPT (see Fig. 4.14). Furthermore, the alignment of the grains in deformation direction is clearly visible in both cases as well. The large hardness increase in the

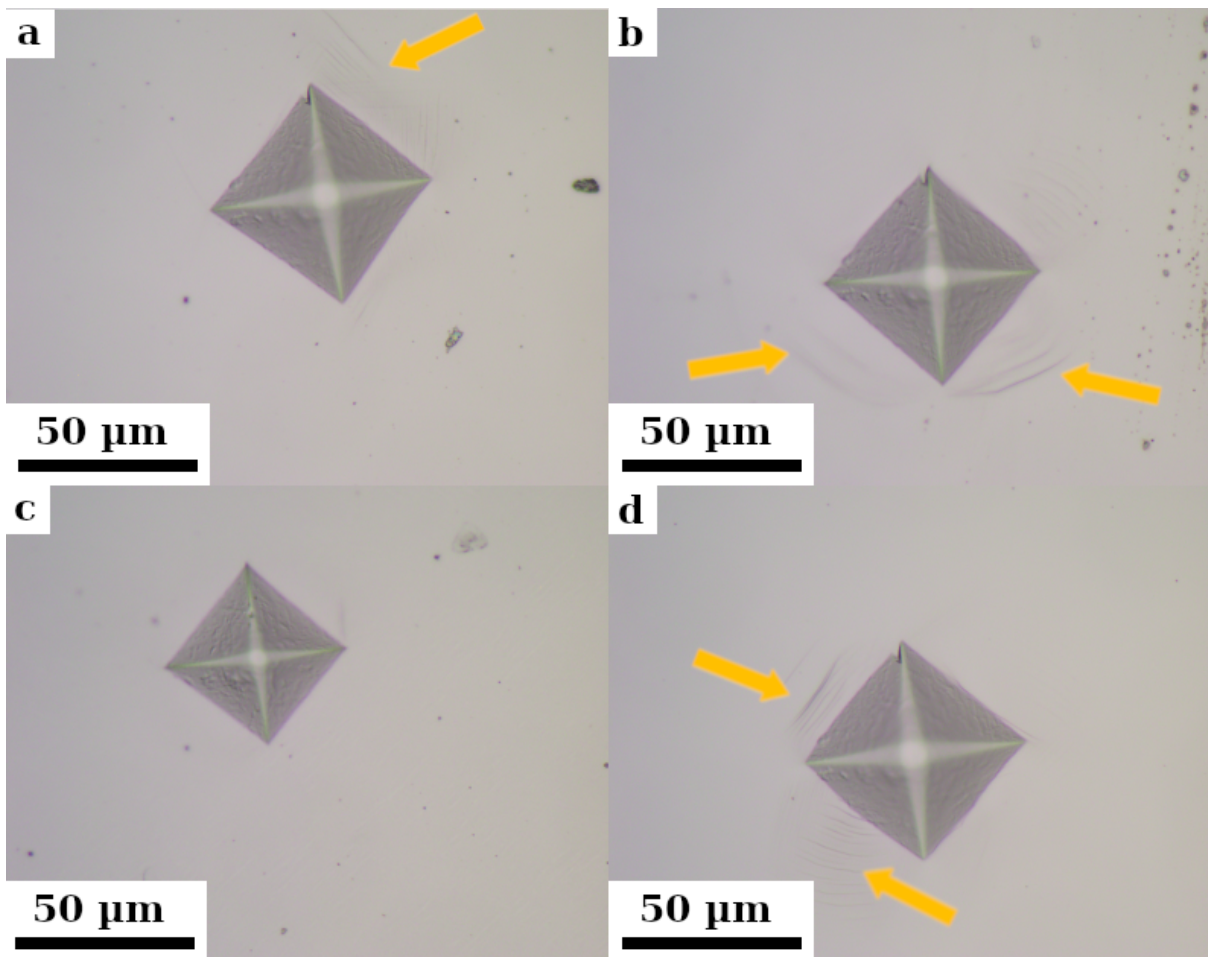


Figure 4.12: Hardness indents left by HV1 hardness tests at the surface of $\text{Al}_{20}\text{Ti}_{30}\text{Mn}_{10}\text{Nb}_{20}\text{V}_{20}$ samples in the a) as-cast, b) aged (600°C), c) aged (750°C), and d) heated and quenched state. The arrows indicate lines around the hardness indent. These lines might either be cracks or they might be caused by bulging due to plastic deformation.

annealed sample would suggest a major change of the microstructure, which, however, was not observed in the SEM. Therefore, imaging with higher resolution, such as TEM, might be necessary.

4.3.7 Summary

At ambient temperatures this alloy consists of two phases, a B2 majority phase and a hcp minority phase. The hcp phase exists primarily around the grain boundaries owning a jagged morphology, but also within the grains as needle-like precipitates. The appearance and distribution of the needle-like precipitates suggest a orientation relation, as there seem to be only certain, repeating angles within a grain. Further research with EDSB might be able to confirm or disprove this hypothesis. Also, TEM could be employed to explore the degree of order of the B2 phase.

Hardness of AlTi₃₀Mn₁₀NbV after HPT

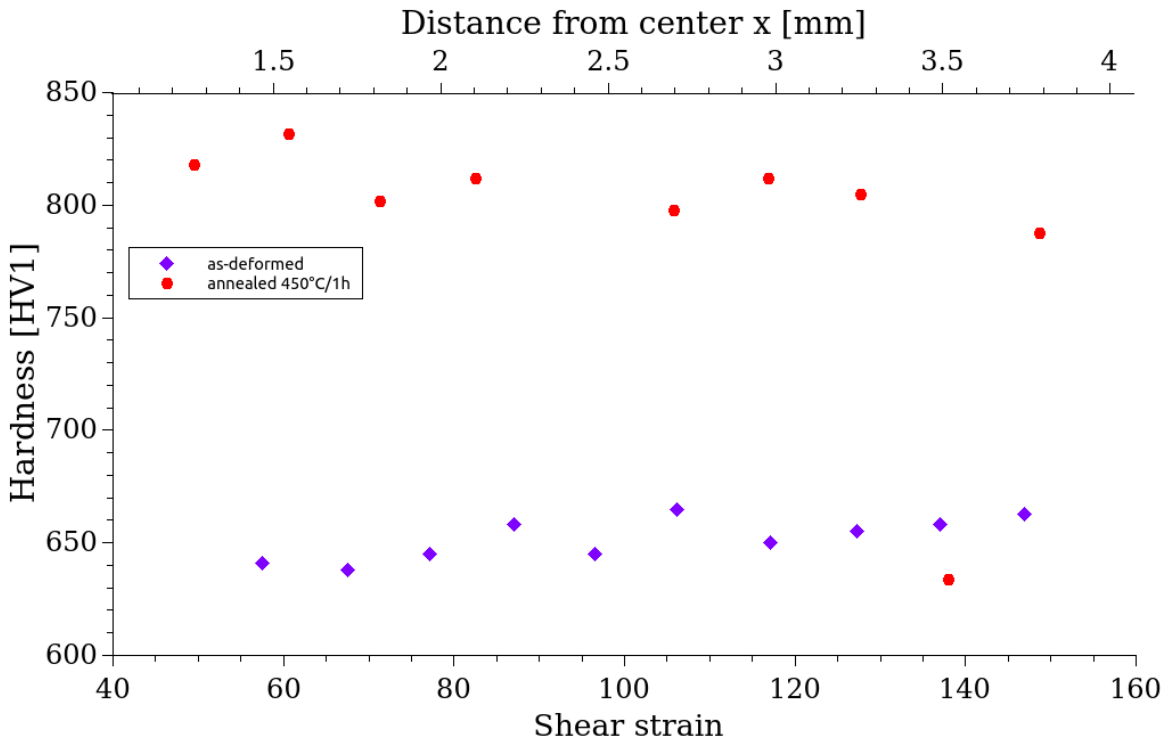


Figure 4.13: Hardness of the Al₂₀Ti₃₀Mn₁₀Nb₂₀V₂₀ alloy as function of the shear-strain for both the as-deformed and annealed state.

A solvus temperature of 1006°C was determined, above which the alloy exists as a single-phase material with a B2 crystal structure, although it is possible that there is a order-disorder transition into a bcc structure at higher temperature, this could be investigated with high temperature XRD in further research. By means of a sufficiently fast cooling rate, the single-phase structure was brought into a metastable state at room temperature. To complement this, it was tested if air quenching is rapid enough to bring the single-phase state down to room temperature. In the SEM it was found that the material only shows a single phase after this heat treatment. However, a dark and a light contrast can be found within each grain, suggesting local differences in chemical composition.

Heating experiments for 24 h have shown, that with increasing temperatures up to 900°C a decomposition of the single phase occurs. At 600°C a very thin grain boundary phase forms. At 750°C an additional fine phase is precipitated within the grains. Finally, at 900°C, the equilibrium microstructure, as described at the beginning of the chapter, is obtained.

While this alloy has a problem with its stability at higher temperatures, thus limiting the application temperature, it could still be an interesting candidate for further research.

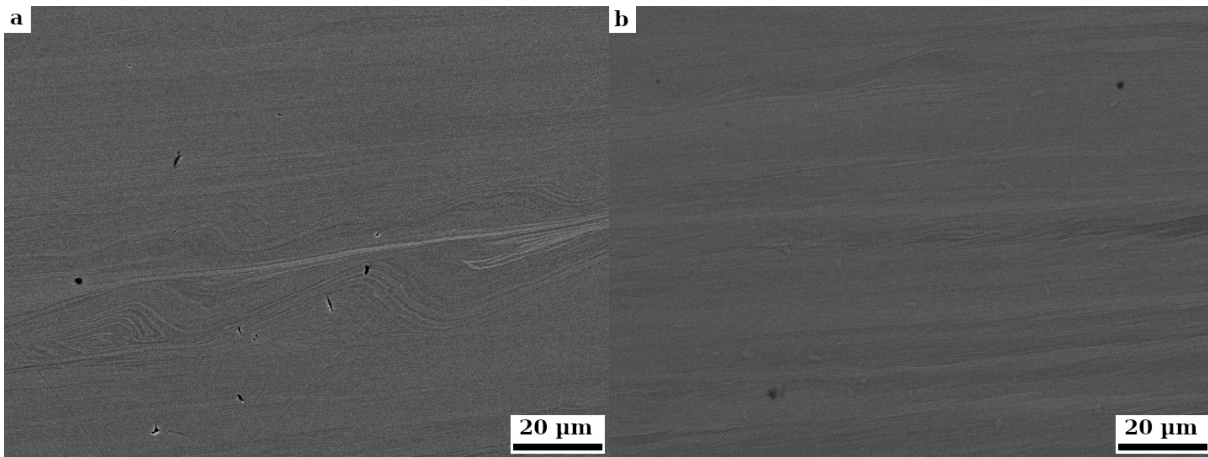


Figure 4.14: SEM-BSE image of $\text{Al}_{20}\text{Ti}_{30}\text{Mn}_{10}\text{Nb}_{20}\text{V}_{20}$ a) after HPT and b) after HPT and annealing at 450°C for 1 hour, followed by air-cooling.

Not only because of the possibility to create a solid solution at room temperature, but also because the microstructure contains fine precipitates, which was obtained by annealing at 750°C . These fine precipitates seem to have improved the mechanical properties, as indicated by the results of the hardness tests.

4.4 $\text{Al}_{20}\text{Ti}_{10}\text{Mn}_{30}\text{Nb}_{20}\text{V}_{20}$

4.4.1 Microstructure and stability

This alloy shows a two-phase microstructure, containing large, globular grains surrounded by a secondary phase in the as-cast state. This was observed in the SEM and can be seen in Fig. 4.15. After a diffusion heat treatment at 900°C no changes other than grain growth were observed. EDX measurements of the annealed sample concluded that one phase is rich in V and contains very little Nb, while, in contrast, the other phase contains an increased amount of Mn and a decreased amount of V, see Tab. 4.10.

Table 4.10: Chemical compositions in atomic percent of the $\text{Al}_{20}\text{Ti}_{10}\text{Mn}_{30}\text{Nb}_{20}\text{V}_{20}$ alloy and the present phases. The labeling of the phases corresponds to that shown in Fig. 4.15d.

	Al	Ti	Mn	Nb	V
Nominal composition	20	10	30	20	20
Measured	20.78	10.09	29.91	20.26	18.96
Phase 1	15.5	6.33	42.51	22.82	12.85
Phase 2	14.9	6.32	32.74	1.11	44.93

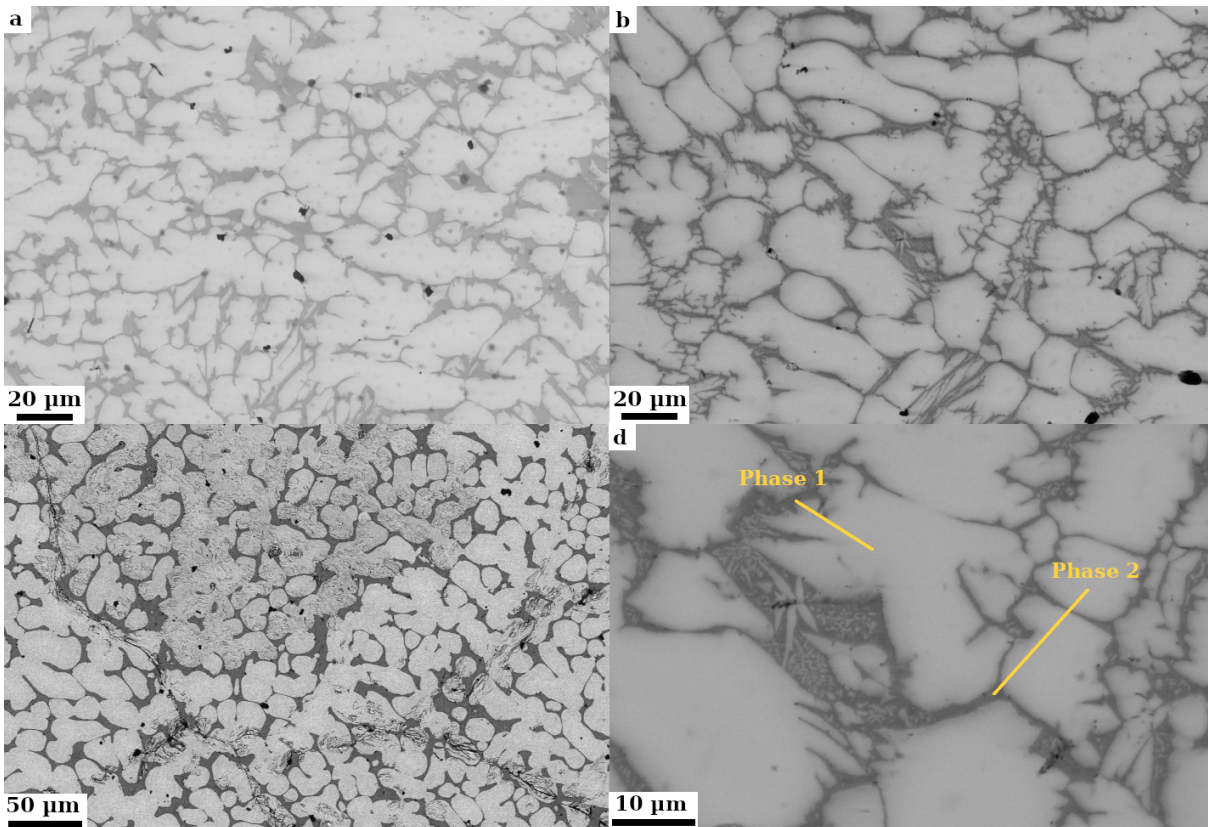


Figure 4.15: SEM-BSE images of $\text{Al}_{20}\text{Ti}_{10}\text{Mn}_{30}\text{Nb}_{20}\text{V}_{20}$ in the a) as-cast, b) homogenized state and c) after heating to 1100°C and water quenching.

4.4.2 Crystal structure analysis

XRD measurements on the as-cast state reveal the existence of a bcc phase with a lattice parameter of 3.20 \AA and a hcp phase with lattice parameters of $a=5.00$ and $c=8.10 \text{ \AA}$. The corresponding XRD pattern can be seen in Fig. 4.16.

Again, the light contrasted phase corresponds to the hcp phase while the bcc phase appears darker in the SEM-BSE images, analogous to AlTiMnNbV and $\text{Al}_{20}\text{Ti}_{30}\text{Mn}_{10}\text{Nb}_{20}\text{V}_{20}$.

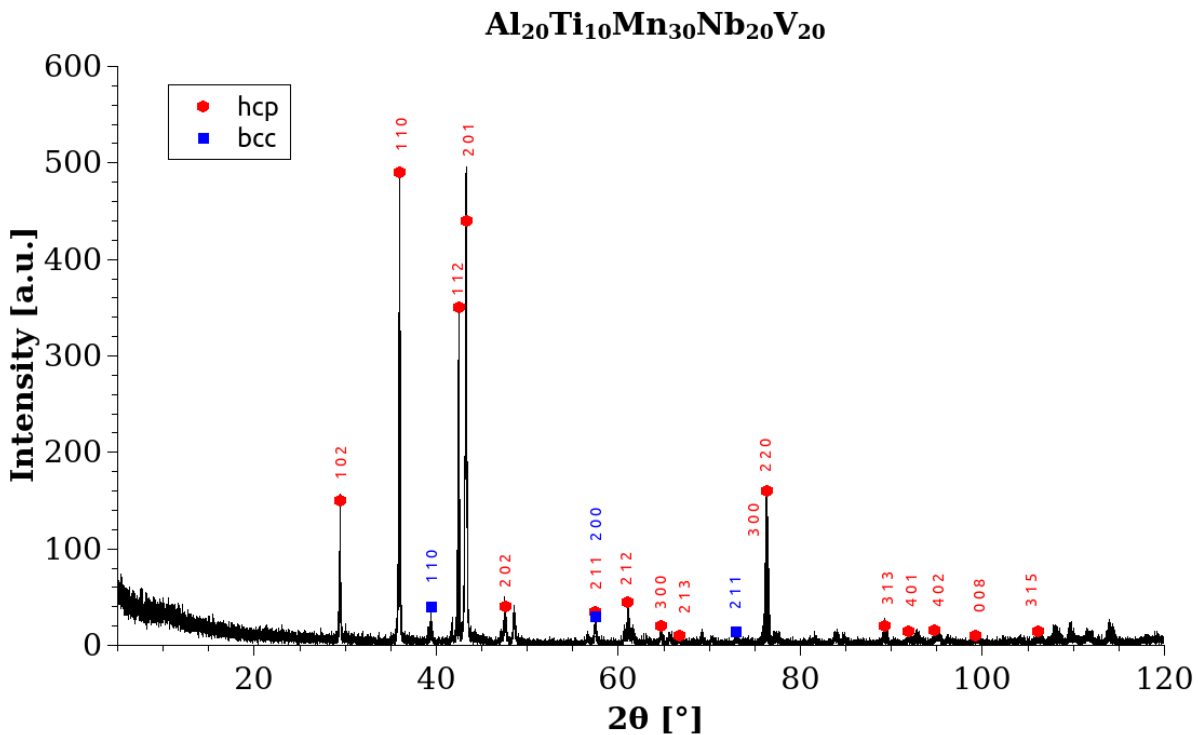


Figure 4.16: XRD diffractogram of the Al₂₀Ti₁₀Mn₃₀Nb₂₀V₂₀ alloy in the homogenized state.

4.4.3 Thermal analysis

In a DSC experiment, the sample was heated to a temperature of 1600°C in order to find out if a transition to a single phase occurs and to determine the melting temperature. A single exothermic peak was found at a temperature of approximately 990°C. Since the sample did not melt within the crucible, the exothermic peak can only correspond to a phase transition. The DSC curve for this experiment can be found in the appendix (see Fig. 5.5).

4.4.4 Stabilization of a single phase

The next step was to bring the single-phase microstructure down to room temperature. For this, the alloy was heated to a temperature of 1100°C, held for two hours and then quenched in water.

SEM analysis concluded that there was a slight change in microstructure (see Fig. 4.15c) when compared to the homogenized state, but no change of the composition took place. The microstructure changed from many individual grains of the hcp phase, with jagged borders, to a more continuous network of hcp grains with straight phase boundaries within the bcc matrix phase.

An expected result would be that the volume fraction of the phases change after this heat treatment compared to the state before the heat treatment. This, however, was not observed. This could mean that the holding-time was too short, the cooling rate too low or that the reaction at that temperature, which was indicated by the DSC measurement, does not correspond to a transition temperature which leads to a single-phase field region.

4.4.5 Density and hardness

The density of this alloy was found to be 6.5 g/cm^3 . No hardness testing was conducted on this alloy.

4.4.6 Summary

At room temperature this alloy consists of hcp and a bcc phases. It was not possible to create a single-phase material by heating and quenching, although a possible solvus temperature was observed. If future research is performed on this alloy, high-temperature XRD could be employed to clarify the question if this alloy changes to a single-phase material at high temperatures or not.

The strong oxidation reaction, the limited sample material and the high Mn content were reasons enough not to increase the holding time at high temperatures or to continue the experiments in the dilatometer (where a faster cooling rate could be achieved), but rather to terminate the research on this alloy as the first impressions seem rather unpromising.

4.5 Further thoughts on the $\text{AlTi}_x\text{Mn}_y\text{NbV}$ system

Three alloys with varying Mn and Ti content were tested in this work. Some observations regarding the chemical composition of the alloys will be presented in this separate section.

As could be seen in the results of the individual alloys, when the alloy is in a decomposed state the microstructure consists of a bcc (B2) and hcp phase in all three cases. Although no superlattice reflections could be identified for alloys other than $\text{Al}_{20}\text{Ti}_{30}\text{Mn}_{10}\text{Nb}_{20}\text{V}_{20}$, it is believed that the other alloys show some degree of long-range order as well. As we go from low Mn concentrations to equiatomic and finally to

high Mn concentrations, the phase fraction goes from a mostly bcc (B2) to a balanced and finally to a mostly hcp microstructure, as can be seen in Fig. 4.17. Out of the three alloys only the alloy with higher Ti content exhibits a single-phase state.

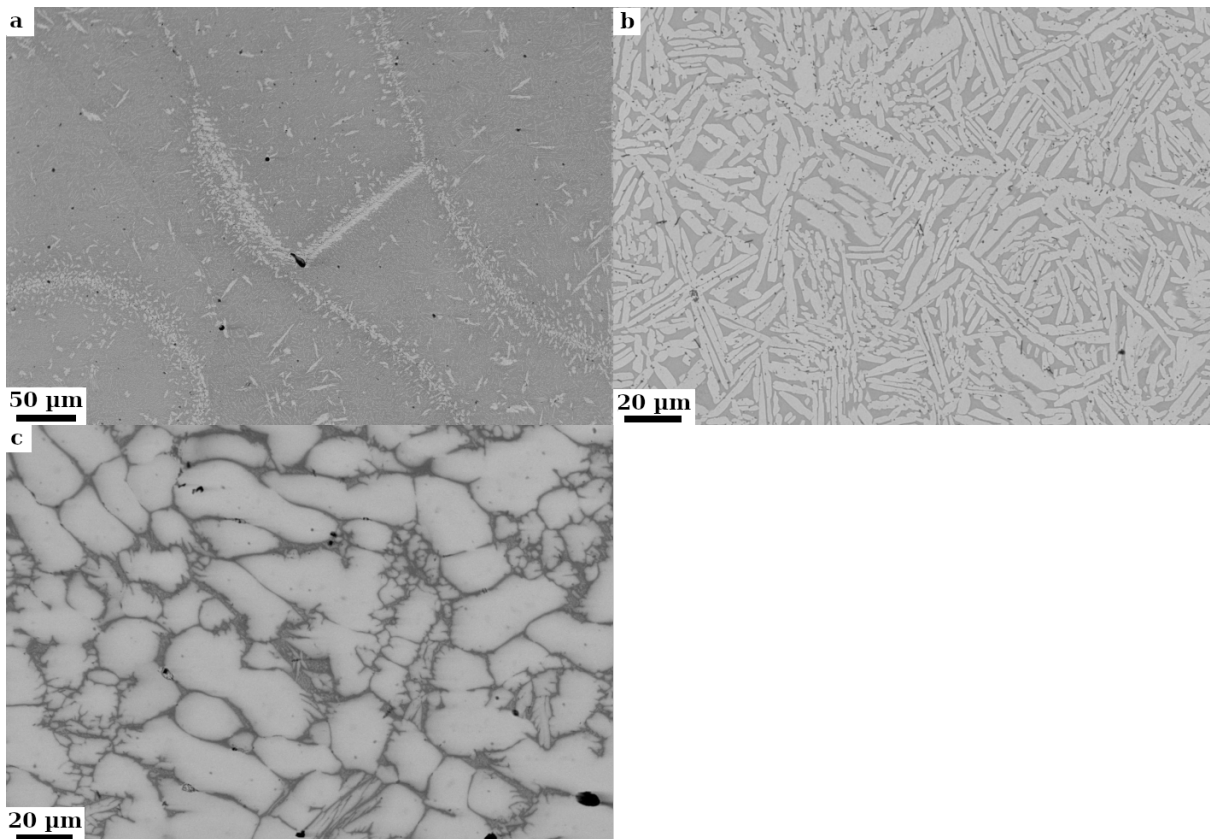


Figure 4.17: SEM-BSE images of a) $\text{Al}_{20}\text{Ti}_{30}\text{Mn}_{10}\text{Nb}_{20}\text{V}_{20}$, b) AlTiMnNbV and c) $\text{Al}_{20}\text{Ti}_{10}\text{Mn}_{30}\text{Nb}_{20}\text{V}_{20}$ in a homogenized, decomposed state.

Taking this microstructural evolution into account, it is expected that an even higher Mn content could lead to a formation of a single-phase alloy with hcp structure. A decrease in Mn could lead to a higher phase fraction of the bcc-phase until a Mn content of 0% is reached the AlTiNbV system is arrived, which again is forming a single-phase material, as previously described by B. Schuh et al. [22]. In addition, this alloy system was identified to form a B2 phase as reported by Yurchenko et al. [19].

Another unknown variable is the role that the alloying elements, other than Ti and Mn, play in stabilizing a solid solution. From the various EDX measurements it is evident, for instance, that V always seems to prefer the the bcc (B2) phase, while Nb seems to prefer the hcp phase. This could be used as an advantage when trying to increase the thermodynamic stability of a chosen phase via alloy composition.

Going forward, CALPHAD could be used to calculate a quasi-binary phase diagram for this system, which would be useful to predict phase transitions and could help further

alloy development. Also, ab-initio calculations could be employed to find the most stable composition of the $\text{AlTi}_x\text{Mn}_y\text{NbV}$ system.

5 Conclusions

In the present master thesis four different high-entropy alloys were investigated with a focus on their ability to form a solid solution, the crystallography of the present phases as well as their stability and response to heat treatments. The base elements of the alloys are Al, Ti, Nb, V and in addition Mn or Mo. While for the Mo containing variant only an equiatomic alloy was investigated, three different Mn containing variants were examined. Out of the four alloys only the Mo variant, with the nominal composition of $\text{Al}_{20}\text{Ti}_{20}\text{Mo}_{20}\text{Nb}_{20}\text{V}_{20}$, and the Mn_{10} variant with the nominal composition of $\text{Al}_{20}\text{Ti}_{30}\text{Mn}_{10}\text{Nb}_{20}\text{V}_{20}$ showed promising tendencies to form a stable solid solution.

After heat treatments for 24 h at temperatures up to 1200°C it was found that only the Mo variant was stable with no visible microstructural change other than grain growth. The Mn variants, on the other hand, showed different responses, depending on the temperature and cooling rate, but ultimately it was shown that this alloy does not form a stable single-phase solid solution at temperatures lower than the solvus temperature of around 1006°C, but rather decompose into a hcp and a B2 phase.

With all the mentioned results in mind it can be concluded that the Mo containing alloy shows the most promising properties, especially when considered high-temperature applications. For the Mn containing alloy it seems that a lower Mn content can lead to a increased stability of a single-phase solid solution. Even though the alloys do not exist as a thermodynamic stable solid solution, a metastable single-phase state could be achieved with the $\text{Al}_{20}\text{Ti}_{30}\text{Mn}_{10}\text{Nb}_{20}\text{V}_{20}$ alloy by accelerated cooling after heating the sample above the solvus temperature.

The final conclusion of this thesis can be summed up as following:

1. AlTiMoNbV is a promising prospect for high-temperature applications but needs a more reliable manufacturing method as well as additional research and characterization with high resolution methods, such as TEM and APT.
2. The $\text{AlTi}_x\text{Mn}_y\text{NbV}$ system shows promising properties, but needs further development work to improve the thermodynamic and thermal stability.

Bibliography

- [1] D. B. Miracle and O. N. Senkov, “A critical review of high entropy alloys and related concepts”, *Acta Materialia* **122**, 448–511 (2017).
- [2] Y. Zhang, T. T. Zuo, Z. Tang, M. C. Gao, K. A. Dahmen, P. K. Liaw, and Z. P. Lu, “Microstructures and properties of high-entropy alloys”, *Progress in Materials Science* **61**, 1–93 (2014).
- [3] B. Cantor, I. T. Chang, P. Knight, and A. J. Vincent, “Microstructural development in equiatomic multicomponent alloys”, *Materials Science and Engineering A* **375-377**, 213–218 (2004).
- [4] A. B. Melnick and V. K. Soolshenko, “Thermodynamic design of high-entropy refractory alloys”, *Journal of Alloys and Compounds* **694**, 223–227 (2017).
- [5] Y. Lederer, C. Toher, K. S. Vecchio, and S. Curtarolo, “The search for high entropy alloys: A high-throughput ab-initio approach”, *Acta Materialia* **159**, 364–383 (2018).
- [6] H. W. Luan, Y. Shao, J. F. Li, W. L. Mao, Z. D. Han, C. Shao, and K. F. Yao, “Phase stabilities of high entropy alloys”, *Scripta Materialia* **179**, 40–44 (2020).
- [7] P. W. Atkins and J. de Paula, *Physical Chemistry*, 10th ed. (Oxford University Press, Oxford, United Kingdom, 2017).
- [8] C. G. Schön, T. Duong, Y. Wang, and R. Arróyave, “Probing the entropy hypothesis in highly concentrated alloys”, *Acta Materialia* **148**, 263–279 (2018).
- [9] J. W. Yeh, S. K. Chen, S. J. Lin, J. Y. Gan, T. S. Chin, T. T. Shun, C. H. Tsau, and S. Y. Chang, “Nanostructured high-entropy alloys with multiple principal elements: Novel alloy design concepts and outcomes”, *Advanced Engineering Materials* **6**, 299–303 (2004).
- [10] S. Gorsse, J. P. Couzinié, and D. B. Miracle, “From high-entropy alloys to complex concentrated alloys”, *Comptes Rendus Physique* **19**, 721–736 (2018).
- [11] J. Wang, J. Li, Q. Wang, J. Wang, Z. Wang, and C. T. Liu, “The incredible excess entropy in high entropy alloys”, *Scripta Materialia* **168**, 19–22 (2019).
- [12] I. Toda-Caraballo and P. E. Rivera-Díaz-Del-Castillo, “Modelling solid solution hardening in high entropy alloys”, *Acta Materialia* **85**, 14–23 (2015).
- [13] R. L. Fleischer, “Substitutional solution hardening of copper”, *Acta Metallurgica* **14**, 1867–1868 (1966).

- [14] J. Dąbrowa, M. Zajusz, W. Kucza, G. Cieślak, K. Berent, T. Czeppe, T. Kulik, and M. Danielewski, “Demystifying the sluggish diffusion effect in high entropy alloys”, *Journal of Alloys and Compounds* **783**, 193–207 (2019).
- [15] G. Gottstein, *Materialwissenschaft und Werkstofftechnik*, 4th ed. (Springer Vieweg, Berlin Heidelberg, Germany, 2015), pp. 213–213.
- [16] R Labusch, “A statistical theory of solid solution hardening”, **659**, 659–669 (1970).
- [17] C. Varvenne, A. Luque, and W. A. Curtin, “Theory of strengthening in fcc high entropy alloys”, *Acta Materialia* **118**, 164–176 (2016).
- [18] L. Zhang, Y. Xiang, J. Han, and D. J. Srolovitz, “The effect of randomness on the strength of high-entropy alloys”, *Acta Materialia* **166**, 424–434 (2019).
- [19] N. Y. Yurchenko, N. D. Stepanov, S. V. Zhrebtsov, M. A. Tikhonovsky, and G. A. Salishchev, “Structure and mechanical properties of B2 ordered refractory AlNbTiVZr_x (x = 0–1.5) high-entropy alloys”, *Materials Science and Engineering A* **704**, 82–90 (2017).
- [20] M. F. Ashby, *Engineering Materials 1*, 4th ed. (Butterworth-Heinemann, Oxford, United Kingdom, 2013), p. 353.
- [21] B. Schuh, F. Mendez-Martin, B. Völker, E. P. George, H. Clemens, R. Pippan, and A. Hohenwarter, “Mechanical properties, microstructure and thermal stability of a nanocrystalline CoCrFeMnNi high-entropy alloy after severe plastic deformation”, *Acta Materialia* **96**, 258–268 (2015).
- [22] B. Schuh, B. Völker, V. Maier-Kiener, J. Todt, J. Li, and A. Hohenwarter, “Phase decomposition of a single-phase AlTiVNb high-entropy alloy after severe plastic deformation and annealing”, *Advanced Engineering Materials* **19/4** (2017).
- [23] G. A. Salishchev, M. A. Tikhonovsky, D. G. Shaysultanov, N. D. Stepanov, A. V. Kuznetsov, I. V. Kolodiy, A. S. Tortika, and O. N. Senkov, “Effect of Mn and v on structure and mechanical properties of high-entropy alloys based on CoCrFeNi system”, *Journal of Alloys and Compounds* **591**, 11–21 (2014).
- [24] P. P. Bhattacharjee, G. D. Sathiaraj, M. Zaid, J. R. Gatti, C. Lee, C. W. Tsai, and J. W. Yeh, “Microstructure and texture evolution during annealing of equiatomic CoCrFeMnNi high-entropy alloy”, *Journal of Alloys and Compounds* **587**, 544–552 (2014).
- [25] E. J. Pickering, R. Muñoz-Moreno, H. J. Stone, and N. G. Jones, “Precipitation in the equiatomic high-entropy alloy CrMnFeCoNi”, *Scripta Materialia* **113**, 106–109 (2016).

- [26] K. Edalati and Z. Horita, “A review on high-pressure torsion (HPT) from 1935 to 1988”, *Materials Science and Engineering A* **652**, 325–352 (2016).
- [27] H. Zhou, M. Peterlechner, S. Hilke, D. Shen, and G. Wilde, “Influence of plastic deformation by high-pressure torsion on the crystallization kinetics of a Pd40Ni40P20 bulk metallic glass”, *Journal of Alloys and Compounds* **821** (2020).
- [28] P. Verleysen and H. Lanjewar, “Dynamic high pressure torsion: A novel technique for dynamic severe plastic deformation”, *Journal of Materials Processing Technology* **276**, 116393 (2020).
- [29] N. D. Stepanov, D. G. Shaysultanov, G. A. Salishchev, and M. A. Tikhonovsky, “Structure and mechanical properties of a light-weight AlNbTiV high entropy alloy”, *Materials Letters* **142**, 153–155 (2015).
- [30] N. D. Stepanov, N. Y. Yurchenko, D. V. Skibin, M. A. Tikhonovsky, and G. A. Salishchev, “Structure and mechanical properties of the AlCr_xNbTiV (x = 0, 0.5, 1, 1.5) high entropy alloys”, *Journal of Alloys and Compounds* **652**, 266–280 (2015).
- [31] A. Lacour-Gogny-Goubert, Z. Zhao-Huvelin, A. Bachelier-Locq, I. Guillot, and A. Denquin, “Effect of Al content on microstructure and properties of Al_xMoNbTiV RCCA’s alloys”, *Materials Science Forum* **941**, 1111–1116 (2018).
- [32] D. Choudhuri, B. Gwalani, S. Gorsse, C. V. Mikler, R. V. Ramanujan, M. A. Gibson, and R. Banerjee, “Change in the primary solidification phase from fcc to bcc-based B2 in high entropy or complex concentrated alloys”, *Scripta Materialia* **127**, 186–190 (2017).
- [33] N. W. Ashcroft and D. N. Mermin, *Solid State Physics (Festkörperphysik)*, 3rd ed. (Oldenbourg Wissenschaftsverlag GmbH, München, Germany, 2007).
- [34] B. Warren, *X-Ray Diffraction*, 1st ed. (Dover, New York, United States of America, 1990), p. 21.

Appendix

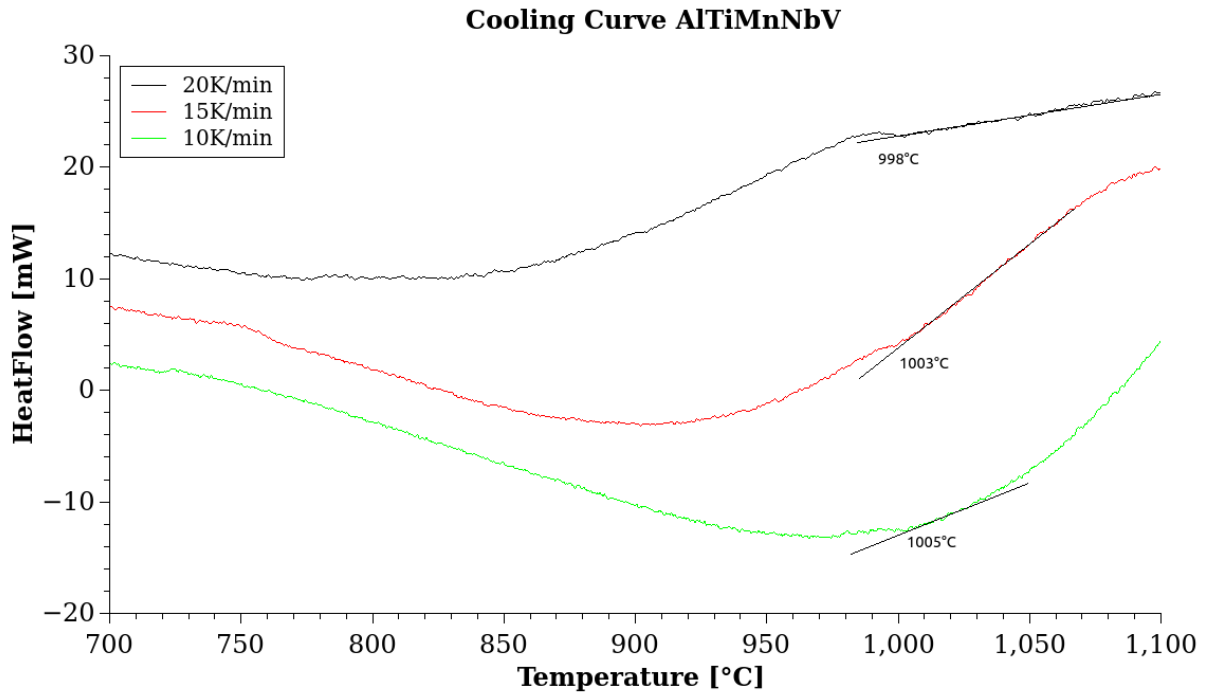


Figure 5.1: DSC measurements of the AlTiMnNbV alloy using heating and cooling rates of 20 to 10 K/min.

Table 5.1: List of density measurements for the individual alloys. Note, that for $\text{Al}_{20}\text{Ti}_{30}\text{Mn}_{10}\text{Nb}_{20}\text{V}_{20}$ and $\text{Al}_{20}\text{Ti}_{10}\text{Mn}_{30}\text{Nb}_{20}\text{V}_{20}$ two independent measurements were performed.

Alloy	Mass m [g]	Volume V [cm ³]	Density ρ [g/cm ³]
AlTiMoNbV	43.99	8.8	5.0
AlTiMnNbV	14.61	2.7	5.5
$\text{Al}_{20}\text{Ti}_{30}\text{Mn}_{10}\text{Nb}_{20}\text{V}_{20}$	14.69	2.7	5.4
$\text{Al}_{20}\text{Ti}_{30}\text{Mn}_{10}\text{Nb}_{20}\text{V}_{20}$	14.63	2.8	5.2
$\text{Al}_{20}\text{Ti}_{10}\text{Mn}_{30}\text{Nb}_{20}\text{V}_{20}$	37.00	5.9	6.3
$\text{Al}_{20}\text{Ti}_{10}\text{Mn}_{30}\text{Nb}_{20}\text{V}_{20}$	20.98	3.1	6.8

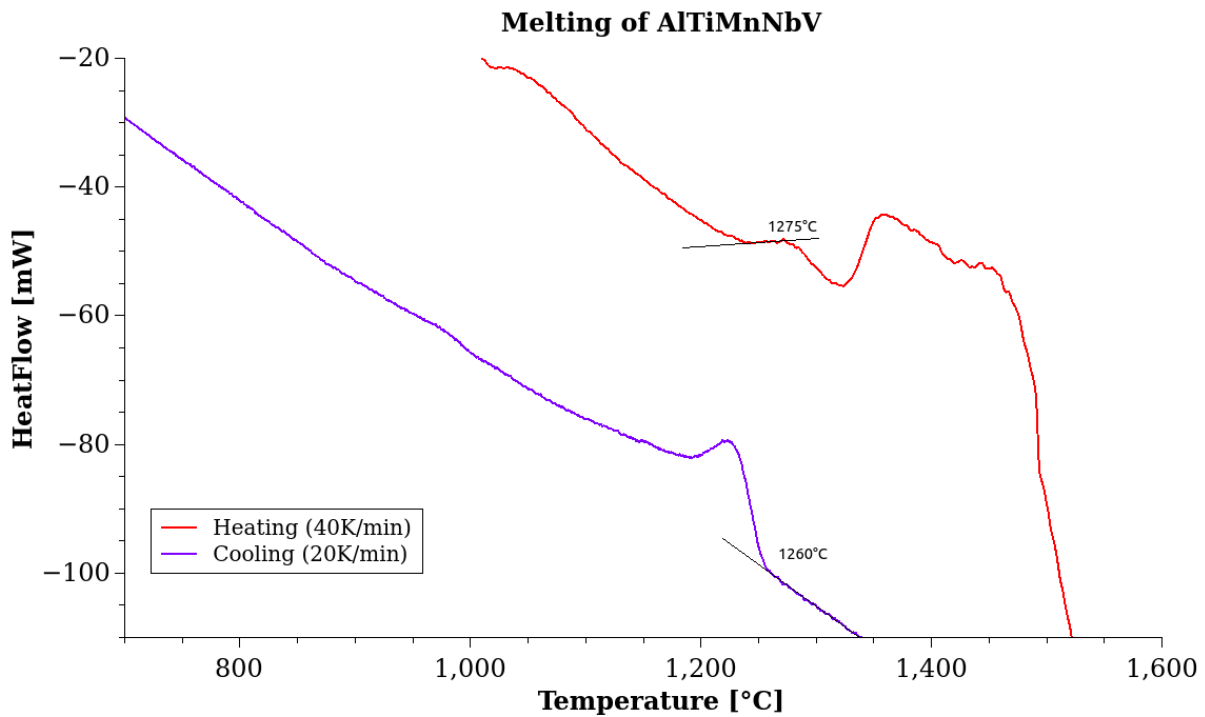


Figure 5.2: DSC measurement of the AlTiMnNbV alloy using heating and cooling rates of 20 K/min. The endothermic and exothermic peaks for melting and fusion are clearly visible. The melting temperature was determined to be about 1275°C.

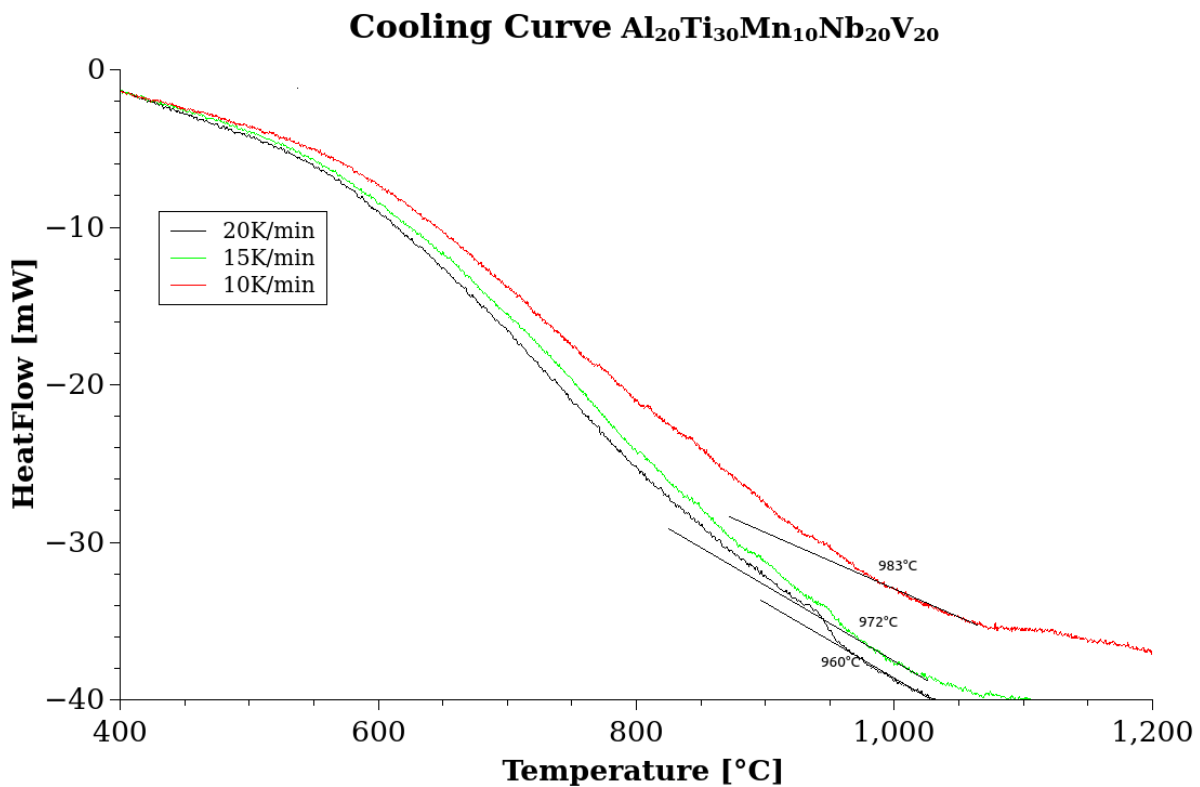


Figure 5.3: DSC measurements of the Al₂₀Ti₃₀Mn₁₀Nb₂₀V₂₀ alloy using heating and cooling rates of 20 to 10 K/min. This measurement was conducted on a sample which was already in a decomposed state.

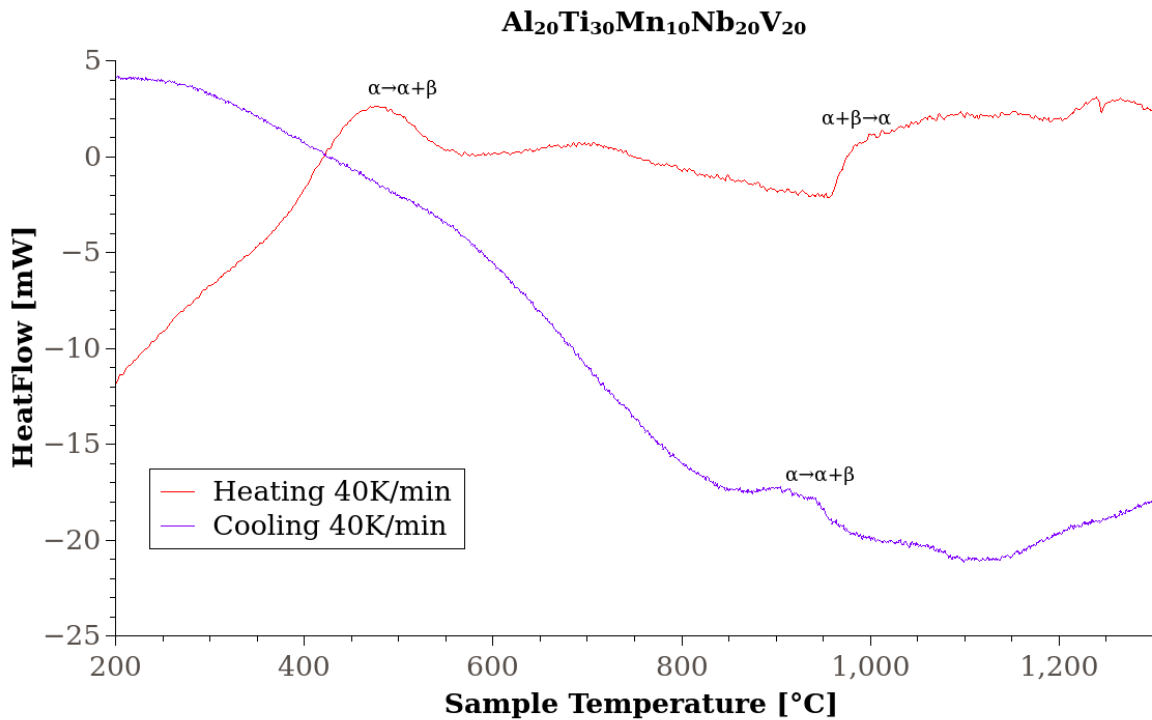


Figure 5.4: DSC measurements of the Al₂₀Ti₃₀Mn₁₀Nb₂₀V₂₀ alloy using a heating rate of 40 K/min and cooling rate of 20 K/min. This measurement was performed starting from the single-phase solid solution. As described in the figure itself, phase transitions are visible. α describes the BCC phase and β describes the HCP phase. During heating the first transition peak corresponds to the decomposition while the second peak corresponds to the transition to a solid solution. During cooling only one peak is observed which corresponds to the formation of the secondary phase.

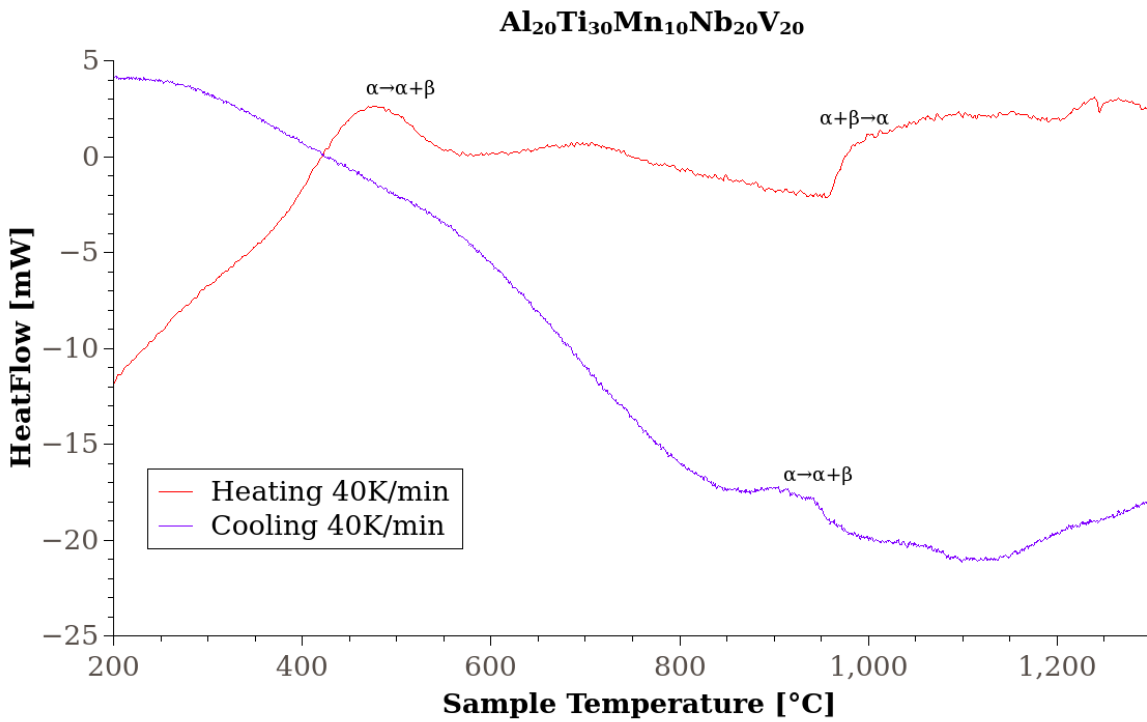


Figure 5.5: DSC measurements of the $\text{Al}_{20}\text{Ti}_{10}\text{Mn}_{30}\text{Nb}_{20}\text{V}_{20}$ alloy using a heating rate of 40 K/min and cooling rate of 20 K/min. This measurement was performed starting from the two-phase homogenized state. The peak observed at around 992°C is believed to correspond to the solvus temperature.

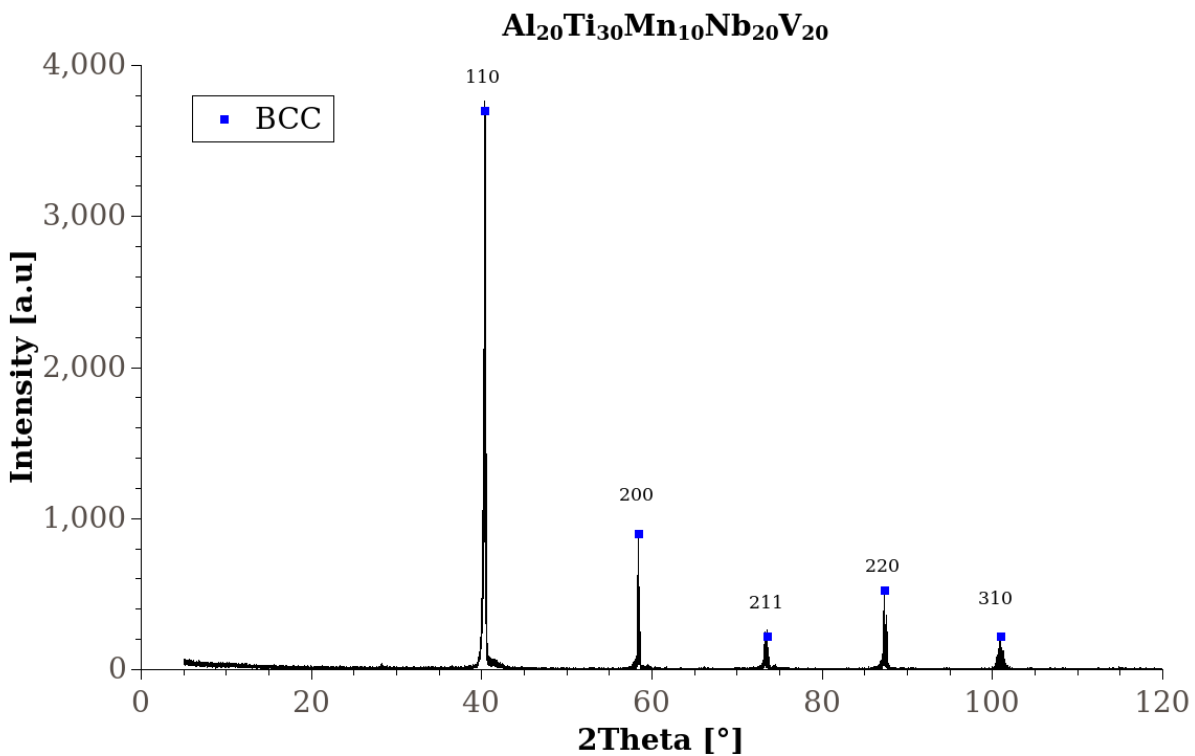


Figure 5.6: XRD diffractogram of the $\text{Al}_{20}\text{Ti}_{30}\text{Mn}_{10}\text{Nb}_{20}\text{V}_{20}$ alloy performed on a single phase as-cast sample that was annealed at 750°C for a total duration of 24 h.

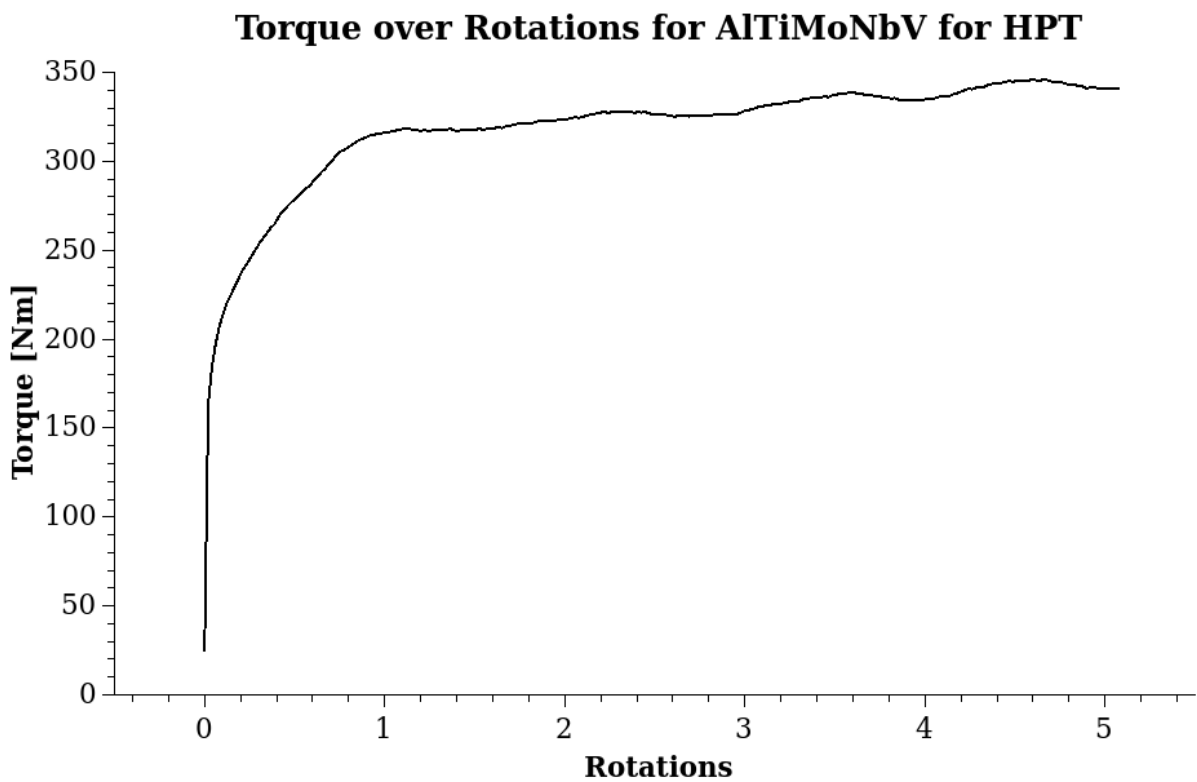


Figure 5.7: Torque as response to HPT as function of the total amount of rotations for the AlTiMoNbV alloy. The slope is representative for the amount of strain hardening. As it is clearly visible, the sample strengthens very quickly during the first revolution, afterwards saturation sets in.

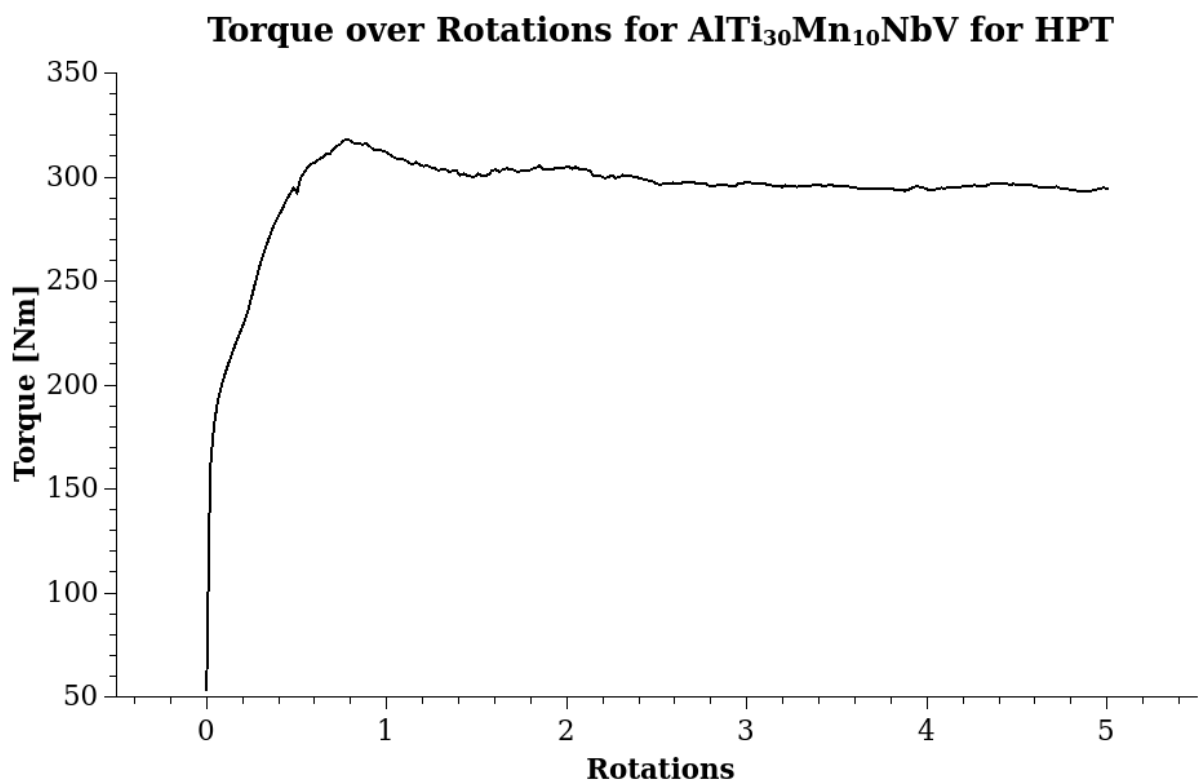


Figure 5.8: Torque as response to HPT as function of the total amount of rotations for the Al₂₀Ti₃₀Mn₁₀Nb₂₀V₂₀ alloy. The slope is representative for the amount of strain hardening. The sample strengthens very quickly during the first revolution, afterwards saturation sets in.